How to Predict Activation Barriers − Conformational Transformations of Compounds $CH_3C(CH_2PPh_2)_{3-n}[CH_2P(oTol)_2]_nMo(CO)_3$ (n = 1−3): Force Field Calculations versus NMR Data

Stefan Beyreuther,[a] Axel Frick,[a] Johannes Hunger,[a] Gottfried Huttner,*[a] Björn Antelmann,[a] Peter Schober,[a] and Rainer Soltek[a]

Dedicated to Prof. Wolf-Peter Fehlhammer on the occasion of his 60th birthday

Keywords: *Tripod* molybdenum tricarbonyl compounds / Conformational analysis in solution / Dynamic NMR / Force field calculations / Activation barriers

Tripod metal entities *tripod*M are sterically congested systems. The conformations adopted by compounds $CH_3C(CH_2PPh_2)_{3-n}[CH_2P(oTol)_2]_nMo(CO)_3$ (n = 1: **1**, n = 2: **2**, n = 3: **3**) will thus be largely determined by the repulsive forces acting in these molecules. The steric demand of the *o*-tolyl groups impedes their free rotation and enantiomerization processes referring to the compounds as a whole are sufficiently slow to permit their analysis by NMR techniques. Through a combination of line-shape analysis, EXSY methods, and coalescence experiments, the $\Delta G^{\ddagger}$ values for these conformational enantiomerization processes have been determined as $\Delta G^{\ddagger}_{298K}$ = 54.3, 57.9, 65.5 kJ·mol^{-1} for compounds **1**, **2**, and **3**, respectively. By an exhaustive search on a force field generated hypersurface, activation energies of 53, 57 and 69 kJ·mol^{-1} have been calculated. Thus, the force field approach correctly reproduces the dependence of the activation energy on the degree of *o*-tolyl substitution. Moreover, the force field simulation also gives an insight into the individual microsteps of the enantiomerization pathways.

Introduction

In any attempt to understand the reactivity of molecules, the shape of the reactants will play an important role. Thus, as far as we know, the reactivity as well as the outstanding selectivity of biological catalysts can, to a large extent, be attributed to the specific shape of the pocket in which the reactive center is embedded. Given appropriate electronic conditions for bond making and bond breaking in a specific catalyst system, the surrounding of the reactive center determines whether or not a substrate will be transformed through its secondary interactions with the latter. In the study of coordination compounds with potential catalytic applications, the electronic situation may nowadays be understood in part by quantum mechanical methods.[1][2]

The secondary interactions, which govern the specific shape of the catalyst as well as of the reactive entity formed upon approach of the substrate at the active site, are not so easy to handle by quantum chemical methods, one problem still being the size of the aggregate formed by a real catalyst and a real substrate. As far as those secondary interactions that are usually referred to as "steric" are concerned, force field methods appear to offer a solution to this problem.[3−7]

There remains a problem, however, when these methods are applied to coordination compounds. Reliable parameters for modelling the interactions involving the metal are generally not available and the only way to obtain an appropriate set of parameters is to gather as much experimental information as possible. If it is desired to develop a force field approach for a specific family of compounds, the structures of the members of this family constitute a valuable piece of information, not only because this information is quite detailed but also because in most cases it is easy to obtain and amply available. It has been shown how this type of information may be systematically analyzed and how, by the application of a combination of statistical tools, including pattern recognition by neural networks, it may be shown for a given family of compounds that, even though the structures have been determined in the solid state, the conformations are almost exclusively determined by the inner molecular potential.[8][9] It has also been shown how this information relating to the molecular potential, intrinsically embedded in these structures, may be extracted in an unbiased way by the use of Genetic Algorithms.[10][11] It has been found that in the specific case of *tripod* metal templates [*tripod* = $RCH_2C(CH_2X)(CH_2Y)(CH_2Z)$; X, Y, Z = $PR'R''$] this two-step process − systematic analysis of the structural database and algorithmic extraction of force field parameters therefrom − makes the force field approach a reliable means of prediction as far as stationary structures are concerned.

It has also been found that the properties of a conformational ensemble, as present for a specific *tripod* metal compound in solution, are adequately reproduced by such a force field approach, in so far as observed NOE distances

[a] Anorganisch-Chemisches Institut der Universität Heidelberg, Im Neuenheimer Feld 270, D-69120 Heidelberg, Germany
Fax: (internat.) + 49-(0)6221/54-5707
E-mail: INVERSION@indi.aci.uni-heidelberg.de

  1434−1948/00/0404−0597 $ 17.50+.50/0

compare favorably with the values predicted on the basis of the force field model.[12] In order to predict NOE distances, a Boltzmann weighted sum has to be taken over all possible conformations and the fact that the observed distances are well reproduced by these model calculations would appear to be supportive of the notion that the relative energies as calculated by the model should be somehow on scale with the experimental reality. NOE measurements thus provide a further valuable piece of information in validating a force field approach.[12]

Experimental data more directly related to the relative energies would provide yet further information. If it were possible to measure the height of the barrier associated with transmutation of a pair of conformers of a given molecule into one another, this barrier height could be compared with the corresponding value calculated by the force field approach.

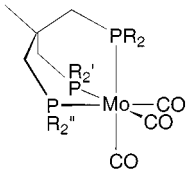

	R	R'	R"
1	*o*Tol	Ph	Ph
2	*o*Tol	*o*Tol	Ph
3	*o*Tol	*o*Tol	*o*Tol

Figure 1. Compounds **1**−**3**

This approach is taken in this paper: It is found that the three molecules $CH_3C(CH_2PPh_2)_{3-n}[CH_2P(oTol)_2]_nMo(CO)_3$, $n = 1$: **1**, $n = 2$: **2**, $n = 3$: **3** (Figure 1) exist in the form of two necessarily isoenergetic conformational enantiomers in solution. These conformers transform into each other by a process that is sufficiently slow to be energetically analyzed by NMR techniques and hence the activation barriers for this process are known for all three compounds. A force field approach, as developed previously,[10,11,12] is used to model these transformations and a highly satisfying agreement between the observed and the calculated energies is found.

Results and Discussion

NMR Analysis

Compounds **1**−**3** (Figures 2, 3, 4) were synthesized by procedures akin to those well-established for the preparation of compounds of this type (see Experimental Section).

Single crystals of sufficient quality could not be obtained for **1** and **2**, so that only the structure of **3** could be determined by X-ray crystallography.[10] NMR data for the compounds were obtained from solutions (**1**, **2**: CD_2Cl_2; **3**: $CDCl_3$) in sealed NMR tubes under argon. An almost complete assignment of all the protons and carbon atoms was achieved by a combination of one- and two-dimensional NMR techniques including DQF-COSY,[13] TOCSY,[14] NOESY,[15] HSQC,[16] and HMBC[17] experiments (Figure 20 and Tables 13 and 14) show the assignment of the

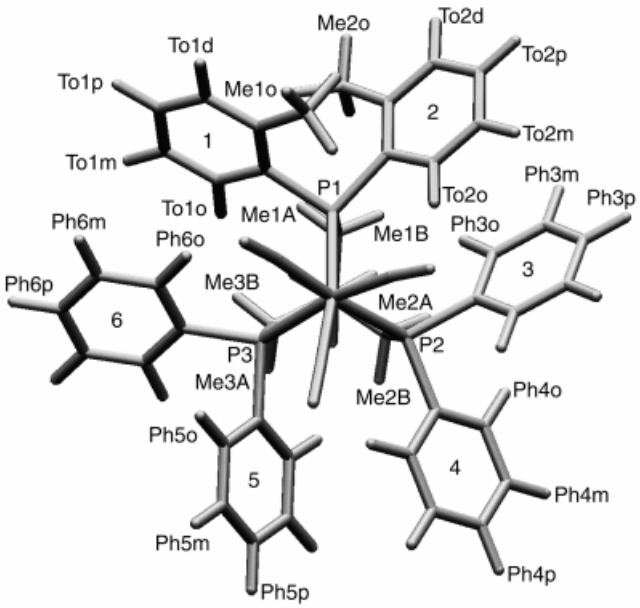

Figure 2. Projection of **1** onto the plane defined by its 3 P atoms; the numbering scheme given here is used throughout in the text

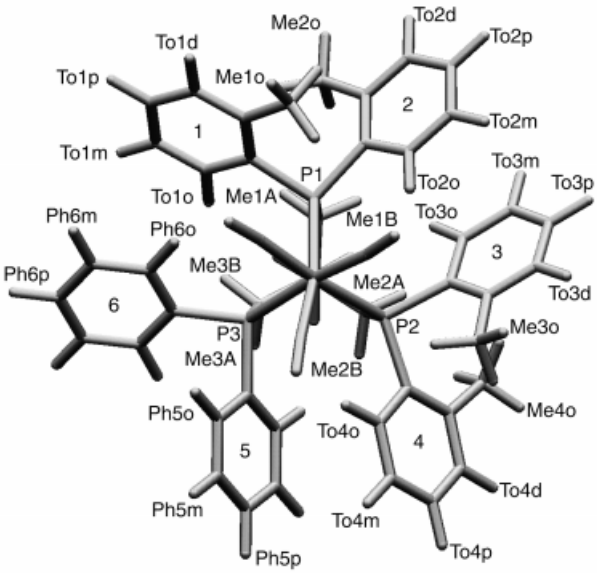

Figure 3. View of the structure of **2** in a projection onto the plane defined by the 3 P atoms; the numbering scheme given here is used throughout the text and tables

^1H and ^{13}C resonances as well as the NOESY, EXSY, and HMBC cross-peaks; see Experimental Section).

It is observed that the phenotype of the spectra changes with temperature. This is exemplified in Figure 5 by focussing on the phosphorus signals of **1** at a few selected temperatures.

At 313 K, only one triplet and one doublet are observed, in accord with the presence of one $P(oTol)_2$ group and two PPh_2 groups. At lower temperatures (Figure 5), a more complicated pattern evolves with the triplet transforming into a doublet of doublets and the doublet splitting into

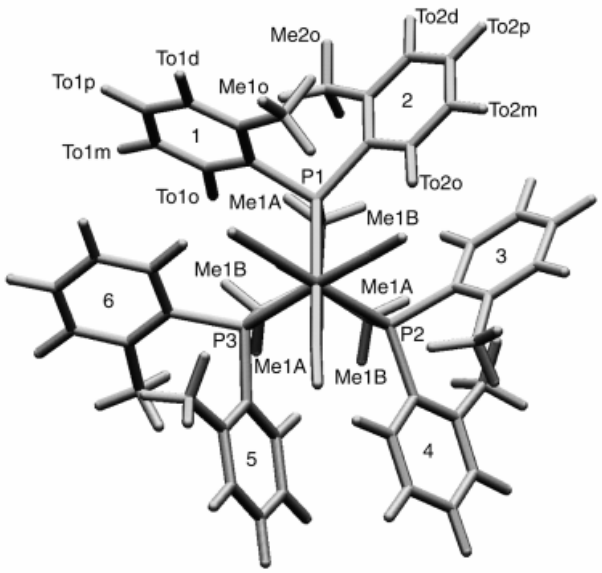

Figure 4. The structure of **3** as projected onto the plane of its 3 P atoms; according to the constitutional C_3 symmetry of the compound, only a subset of atom designators is given; designators for the symmetrically dependent atoms are defined through appropriate reference to the numbers assigned to the phosphorus atoms and the aryl rings as shown in this figure; this numbering scheme is used throughout in the text and tables

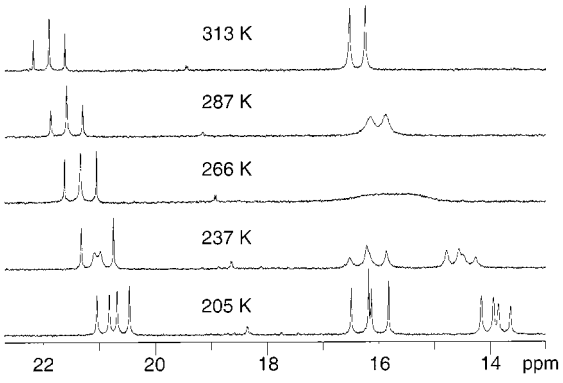

Figure 5. Temperature dependence of the $^{31}P\{^1H\}$-NMR spectrum of **1**; of the 21 spectra collected over the temperature range between 166 K and 313 K, only a few salient examples are shown in the figure; measuring frequency: 81.014 MHz

two such doublet of doublets patterns (Figure 5). The low-temperature spectrum is in accord with a structure of **1** where chiral differentiation between the two PPh_2 groups is static on the NMR time scale. With the shifts and coupling constants given for this type of structure in the legend of Figure 6, the spectrum at the low-temperature limit is correctly reproduced.

The NMR data thus show that there is only one compound present in solution at low temperatures. There remains, however, the possibility that this compound exists as a racemic mixture of two enantiomeric forms.

The ^{1}H-NMR spectra behave accordingly (Figure 7). While the methylene protons, for instance, give rise to a broad unresolved signal at around $\delta = 2.4$ at 293 K, this signal coalesces on cooling and reappears in the form of a

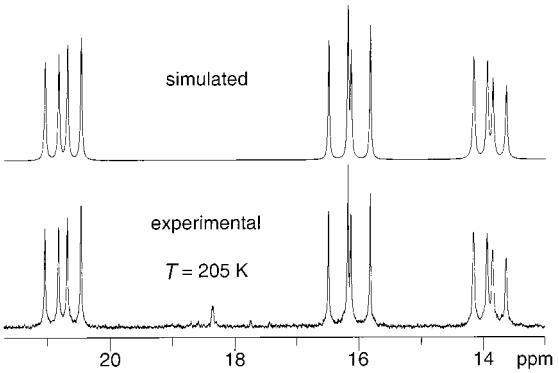

Figure 6. Experimental and simulated $^{31}P\{^1H\}$-NMR spectra of **1** at the low-temperature limit; experimental (bottom) and simulated (top) $^{31}P\{^1H\}$-NMR spectra of **1** at 205 K; $\delta(P1) = 20.75$, $\delta(P2) = 13.91$, $\delta(P3) = 16.15$, $^2J_{P1P2} = 17.8$ Hz, $^2J_{P1P3} = 29.0$ Hz, $^2J_{P2P3} = 25.0$ Hz

complicated multiplet between $\delta = 1.8$ and 2.8. Upon ^{31}P decoupling, this simplifies to a pattern with a minimum of 12 well-resolved lines (Figure 7).

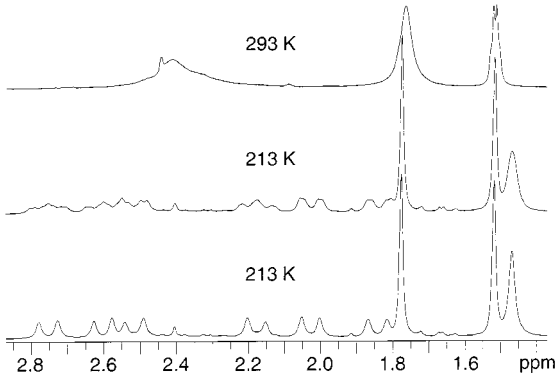

Figure 7. Temperature dependence of the aliphatic region of the ^{1}H-NMR spectrum of **1**; of the 21 spectra collected over the temperature range between 166 K and 313 K, only 3 are shown in the figure; measuring frequency: 300.13 MHz; ^{1}H-NMR spectrum of **1** at 293 K (top), 213 K (middle), and $^1H\{^{31}P\}$-NMR spectrum at 213 K (bottom)

The signal due to the *o*-tolylic methyl groups (Me1o, Me2o, Figure 2) appears as a singlet at around $\delta = 1.8$ at 293 K, which after coalescence is seen as two well-separated sharp singlets at 213 K (Figure 7; from the temperature dependence of these shifts, the center of these two lines can be placed at around $\delta = 1.65$ at 213 K). From this last finding, together with the aforementioned findings from the ^{31}P-NMR data, it is clear that the two methyl groups are in a chemically different environment in the low-temperature structure. Analogous observations have also been made for compounds **2** and **3**, with the different constitutional symmetries of the compounds leading to different appearances of the spectra, although clearly corresponding to the same phenomena. For instance, due to the constitutional equivalence of all three of its $P(o\text{Tol})_2$ groups the ^{31}P-NMR spectrum of **3** shows only one ^{31}P-NMR signal over the entire temperature range. On the other hand, the *o*-tolylic methyl groups as well as the methylene protons of **3** give rise to the

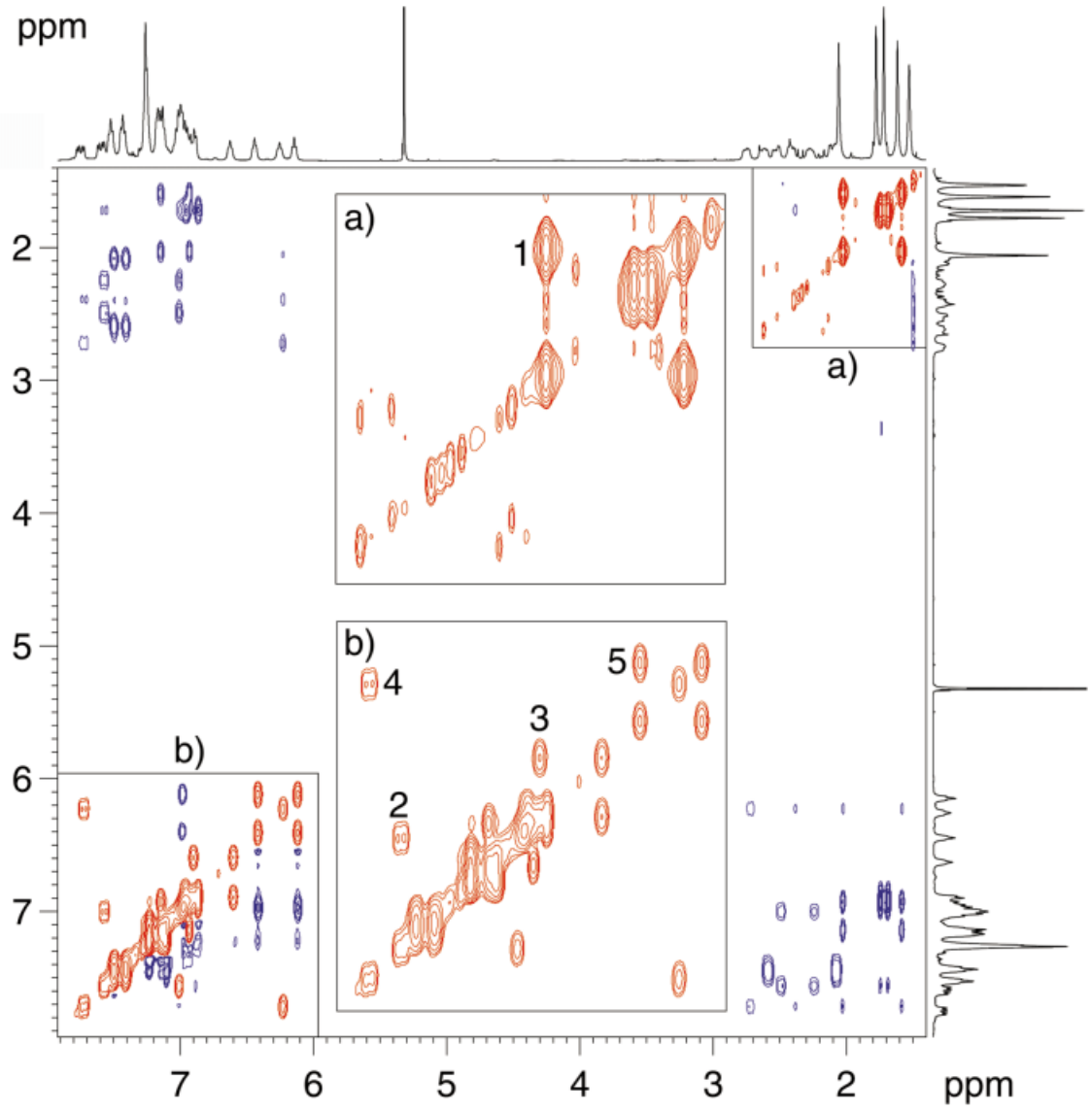

Figure 8. NOESY/EXSY spectrum of **2** at 246 K with a mixing time of 700 ms; measuring frequency: 500.13 MHz; NOESY peaks in blue, EXSY and autocorrelation peaks in red; EXSY peaks are apparent in the methyl, methylene, and arene regions; the EXSY parts of the spectrum between ca. $\delta = 1.5-2.8$ (a) and $\delta = 6.0-8.0$ (b) are shown as enlarged insets; the numbers in these insets refer to the following exchange polarization transfers: 1: Me1o−Me4o, 2: To4o−To1o, 3: To1m−To4m, 4: To2o−To3o, 5: To3m−To2m; designators are as given in Figure 3

same sequence of patterns as seen in the ^{1}H-NMR spectrum of **1**.

If the spectra of **1**−**3** are analyzed for cross-peaks due to dynamic exchange (EXSY) it is observed that the same type of exchange phenomena is present in all cases. This is exemplified by the case of **2** in Figure 8.

The EXSY cross-peaks observed for compounds **1**−**3** are given in Figure 20 and Tables 13 and 14 (see Experimental Section). It can be seen that the *o*-tolyl substituents of each P(*o*Tol)$_2$ group are involved in a mutual exchange. The protons of the CH_2 groups of the backbone of the chelate cage are likewise in a dynamic exchange.

The findings reported thus far show that in each case only one constitutional isomer is present. The observed exchange phenomena must therefore be due to a dynamic exchange between two conformational isomers such that in compound **3**, for instance, Me2o and Me1o as well as Me1A and Me1B etc. (Figures 4, 20) are interchanged in the two different conformeric forms. The most plausible process to account for these observations is a conformational racemization of the compounds, where the torsional arrangement of the aryl groups and the torsion of the chelate cage switch between the image and the mirror image. Figure 9 illustrates this kind of process for the compounds **1**−**3**.

The energy associated with this enantiomerization process has been deduced from relevant NMR observations by three different approaches: (i) Measurement of the coalescence temperature at different field strengths. (ii) Line-shape analysis at different temperatures and field strengths. (iii)

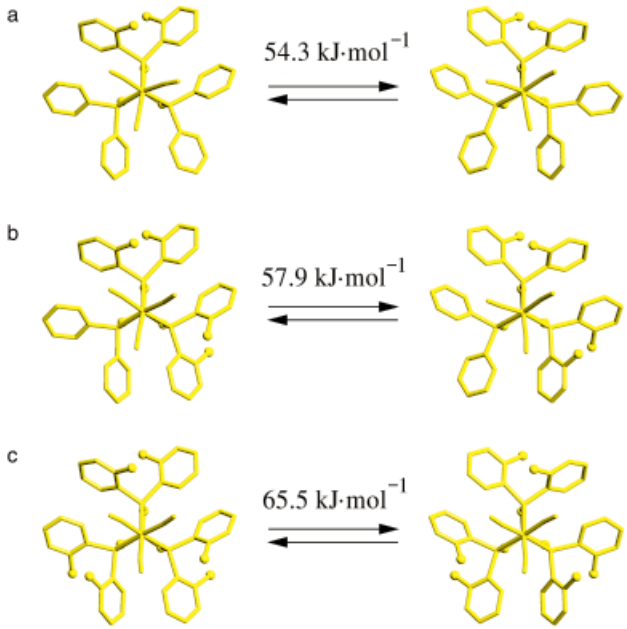

Figure 9. Inversion processes for compounds **1** (a), **2** (b), and **3** (c) and the corresponding experimental $\Delta G^{\neq}_{298K}$ values

Quantification of EXSY data at different temperatures and field strengths. Coalescence experiments have been performed for all three compounds **1**−**3**. Using the phosphorus nuclei as a probe, only **1** and **2** can be analyzed since only one ^{31}P signal is seen for **3** (see Table 12 in the Experimental Section). It is possible, however, to use the ^{1}H signal of the methyl groups of the *o*-tolyl substituents as the analytical tool for all three compounds (**1**−**3**) (Table 1).

Using the methyl protons as the probe, coalescence experiments were performed at various field strengths (Table 1), yielding closely similar results in terms of $\Delta G^{\neq}$ for all the independent experiments in each case (Table 1).

Line-shape analysis[18] of the ^{31}P-NMR data could only be performed for **1** and **2** for the reasons indicated above. As already evident from the case of compound **1** (Figure 5), the shifts are found to be strongly temperature dependent. In order to correct for this temperature dependence, a linear interpolation was used,[19] as is the usual practice. Only very minor additional corrections were found to be necessary for correcting the shift values during refinement.

The quality of fit obtained by the simulation procedure is shown in the insets of Figure 10 for compound **2** at two selected temperatures. The rate constants determined by this procedure should produce a linear plot in an $\ln(k/T)$ vs. $1/T$ diagram (Figure 10), with the slope of the line indicating $\Delta H^{\neq}$ and the abscissa value at $(1/T) = 0$ indicating the activation entropy $\Delta S^{\neq}$.[20] The $\Delta G^{\neq}$ values at 298 K were evaluated as 54.3 kJ·mol^{-1} for **1** ($\Delta H^{\neq}$ = 45.3 kJ·mol^{-1}, $\Delta S^{\neq}$ = −30 J·K^{-1}·mol^{-1}) and 57.9 kJ·mol^{-1} for **2** ($\Delta H^{\neq}$ = 51.8 kJ·mol^{-1}, $\Delta S^{\neq}$ = −20 J·K^{-1}·mol^{-1}) (Table 1).

EXSY spectroscopy constitutes yet another appropriate tool. The exchange phenomena observed pertain to the so-called "equally populated two-site exchange" case, which lends itself to a straightforward analysis by EXSY[15] methods if groups of signals are found which are related to each other solely by exchange and not by coupling.[21] The methyl signals of the *o*-tolyl groups give rise to such sets of signals, so that activation energies can also be derived from EXSY experiments.

If instead of the methyl signals Me1o−Me4o (1, Figure 8) the clearly resolved pairs of signals in the aromatic region e.g. To2m−To3m are used as a probe (5, Figure 8; signals labelled 2, 3, 4 in Figure 8 could also be used), the values

Table 1. Activation energies for the conformational isomerization of **1**−**3**; temperatures in K are given in brackets

Compound	Field [MHz]	$\Delta G^{\neq}_{C(31P)}$ [a] [kJ·mol^{-1}]	$\Delta G^{\neq}_{C(Me)}$ [b] [kJ·mol^{-1}]	$\Delta G^{\neq}_{C(Ar,CH2)}$ [c] [kJ·mol^{-1}]	$\Delta G^{\neq}_{EXSY}$ [d] [kJ·mol^{-1}]	$\Delta G^{\neq}_{LS(31P)}$ [e] [kJ·mol^{-1}]	$\Delta G^{\neq}_{mean}$ [f] [kJ·mol^{-1}]
1	500	54.2 (278)	54.0 (274)	53.9 (274)	52.9 (226)	54.3 (298)	54.4 (298)
	300	54.3 (274)	54.1 (269)	54.1 (269)	51.9 (212)		
	200	53.1 (266)	53.7 (263)	53.6 (263)	52.7 (221)		
2	500	57.8 (297)	58.0 (299)	58.0 (293)	54.8 (224)	57.9 (298)	57.9 (298)
			57.0 (276)				
	300	56.8 (287)	58.1 (293)	56.6 (281)	55.0 (218)		
			56.7 (268)				
	200	56.5 (282)	57.8 (287)	56.9 (277)	55.2 (227)		
			56.8 (261)				
3	200	–	66.6 (338)	65.8 (329)	67.0 (297)	–	65.5 (298)
				65.2 (317)	64.6 (268)		
					64.6 (261)		

[a] ^{31}P{^{1}H}-NMR spectra; coalescence data. − [b] ^{1}H-NMR spectra; coalescence data based on methyl protons. − [c] ^{1}H-NMR coalescence measurements based on arene (**1**−**3**) and CH_2 protons (**3**). − [d] EXSY measurements. − [e] ^{31}P{^{1}H}-NMR line-shape analysis data obtained at three different field strengths: **1**: R^2 = 0.998, $\Delta H^{\neq}$ = 45.3 ± 0.4 kJ·mol^{-1}, $\Delta S^{\neq}$ = −30 ± 1 J·K^{-1}·mol^{-1}; **2**: R^2 = 0.995, $\Delta H^{\neq}$ = 51.8 ± 0.7 kJ·mol^{-1}, $\Delta S^{\neq}$ = −20 ± 2 J·K^{-1}·mol^{-1}; the limits given refer to the estimated standard deviation σ in each case. − [f] Eyring plot constructed from coalescence, EXSY, and line-shape analysis data; **1**: R^2 = 0.995, $\Delta H^{\neq}$ = 45.7 ± 0.5 kJ·mol^{-1}, $\Delta S^{\neq}$ = −29 ± 2 J·K^{-1}·mol^{-1}; **2**: R^2 = 0.990, $\Delta H^{\neq}$ = 48.7 ± 0.7 kJ·mol^{-1}, $\Delta S^{\neq}$ = −31 ± 3 J·K^{-1}·mol^{-1}; **3**: R^2 = 0.986, $\Delta H^{\neq}$ = 59.3 ± 3.5 kJ·mol^{-1}, $\Delta S^{\neq}$ = −21 ± 12 J·K^{-1}·mol^{-1}; the limits given refer to the estimated standard deviation σ in each case; details are given in the Experimental Section.

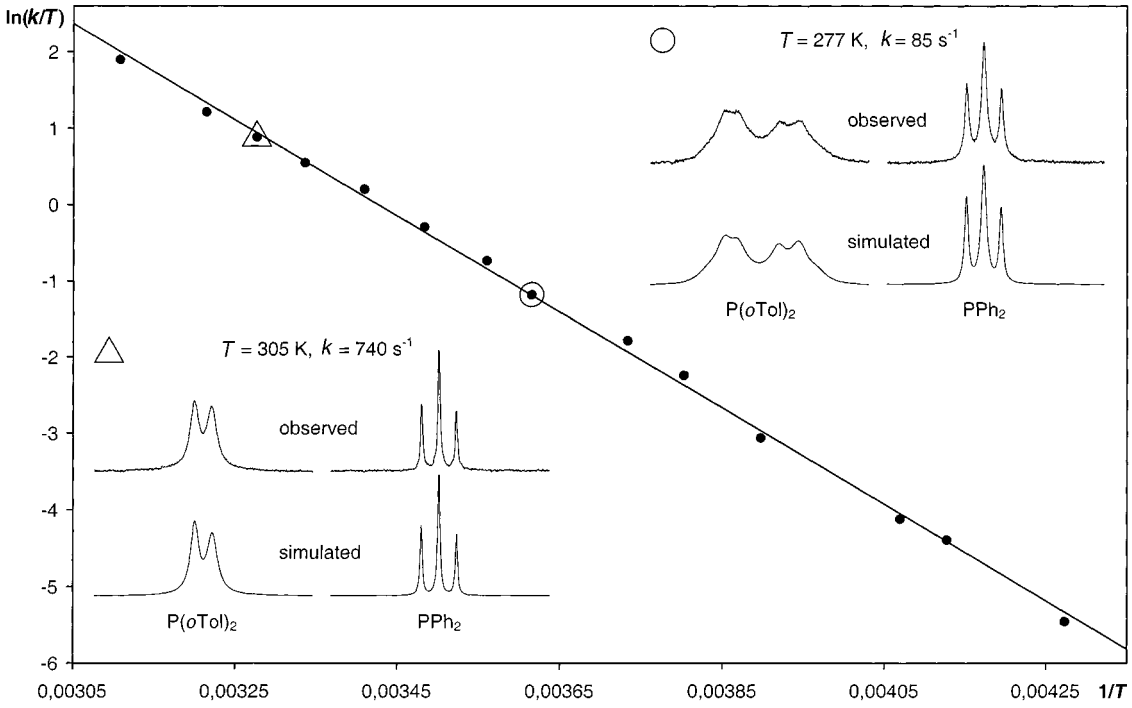

Figure 10. Eyring plot derived from line-shape analysis of compound **2**; the data shown refer to a series of $^{31}P\{^{1}H\}$-NMR measurements taken at 129.495 MHz (^{1}H: 300 MHz); the quality of fit as obtained by the line-shape analysis procedure at the two selected temperatures is indicated in the insets

calculated for the activation barriers remain unchanged as expected.

The activation barriers associated with the conformational enantiomerization of compounds **1**, **2**, **3** are found to increase in the sequence $\Delta H^{\neq} \approx 45,\ 52,\ 59\ kJ{\cdot}mol^{-1}$ (Table 1). On increasing the number of *o*-tolyl groups, the steric congestion increases, making the isomerization process more energy consuming. The activation entropies are found to be negative throughout (**1**: −30; **2**: −20; **3**: −21 $J{\cdot}K^{-1}{\cdot}mol^{-1}$; Table 1). Even though the determination of these activation entropies is based on an extrapolation to $1/T = 0$ in the Eyring diagrams and, owing to the long distance over which this extrapolation has to be taken, is subject to considerable uncertainty, the quality of the data collected suffices to show that the activation entropies are definitely negative. This indicates that the transition state conformations will be even more sterically congested than the ground state conformations. It definitely precludes the hypothesis that the conformational racemization process might occur through decoordination of one of the "legs" of the *tripod* ligand. If this hypothesis were to apply, positive activation entropies would necessarily be observed.

Force Field Model

The force field used to describe compounds **1**−**3** has been derived by global optimization of the relevant force field parameters on the basis of the molecular structures of ten different compounds *tripod*$Mo(CO)_3$ [*tripod* = $RCH_2C(CH_2X)(CH_2Y)(CH_2Z)$; X, Y, Z = PR′R″].[10][11] It has been shown that the conformations adopted by these molecules in the solid state are equilibrium conformations, which are not disturbed to any great extent by the crystal forces.[8][9] In order to derive the relevant force field parameters, those parameters involving contributions from the metal were varied such as to reproduce the observed conformations as local minima on the corresponding energy hypersurfaces. Scaling of the energy was implicitly achieved by using standard MM2* values for all those parameters to which the metal makes no direct contribution. It was not obvious from the outset whether or not the energy scale implicitly defined by the force field parameters would also be appropriate for making energy-based predictions. However, an indication that this is approximately so was provided by the observation that NOE distances are correctly predicted by using the force field generated energies in the exponential terms of a Boltzmann weighting scheme.[12] More direct evidence would be obtained if it were possible to calculate the activation barriers associated with the enantiomerization processes of **1**−**3** and if these values were then found to be close to those observed experimentally in each case.

The experimentally determined activation energies for the conformational racemization processes of compounds **1**−**3** do, in fact, allow a comparison of the energy scale intrinsic to the force field approach with the real world. To this end, a complete reconstruction of the molecular hypersurface by the force field is necessary in order to delineate the least-energy pathway and to finally calculate the activation barrier predicted by this model. Whereas the equilibrium struc-

ture of **3** is more reliable since it has been established by X-ray analysis,[10] the least-energy conformations of **1** and **2** have to be inferred from the force field calculations themselves. This does not, however, appear to be a serious drawback since the structure of **3** as determined by X-ray methods is well reproduced by the force field approach, even as the global minimum on the hypersurface,[10] and since other structures have been predicted with high accuracy by the force field approach taken here.[10] The minimum energy conformations calculated for **1** and **2** are shown in Figures 2 and 3, respectively.

Analysis of 3

With regard to the search for a global minimum on the hypersurface relating to **3**, a complete conformational search has already been carried out, the details of which have been described.[10] It was found that from a starting set of 1376 symmetrically independent conformers, only 262 survived as local minima after refinement based on the *mm2f* parameter set.[10] The conformational space used for the grid search was defined by the six rotations of the aryl groups about their respective P−C_{ipso} bonds.

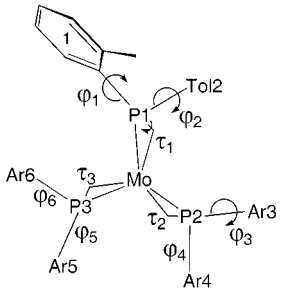

Figure 11. Definition of the six aryl rotations $\varphi_1-\varphi_6$ and the three cage torsions $\tau_1-\tau_3$ used to define the conformational space of compounds **1**−**3**; for the definition of $\varphi = 0°$ see Figure 14; $\tau = 0°$ means that the carbon atom of the bridging CH_2 group would be obscured by the Mo−P line in the diagram

The definition of these rotations denoted as φ is as shown in Figure 11 and is in accord with the definition used previously.[10] The technique used to set these rotations at the values defined by the grid points has also been described previously.[10] The torsion of the chelate cage as described by τ,[8] defined as indicated in Figure 11, was set at a uniform starting value of 20° for all three "legs" of the ligand and it was found that the strain imposed on it by the forced rotation of the aryl groups is sufficiently strong to produce negative as well as positive torsions after refinement.

The energies of the local minima obtained after refinement are distributed as shown in Figure 12a. There are only a few low-energy conformations in the energy band of 20−30 kJ·mol^{-1} above the global minimum. The three conformations with the lowest energy are qualitatively identical (the arrangement of the heavy atoms is designated as 3.1 in Figure 13); the main difference between them stems from a slightly different orientation of the methyl groups of the *o*-tolyl moieties and the energy difference between these almost identical conformers is correspondingly small.

The conformation at position four on the energy scale is already more than 10 kJ·mol^{-1} above the global minimum, with a geometry as shown in Figure 13 (designated as 3.2). This result is well in accord with the observation that in the solid state **3** adopts a conformation corresponding to the global minimum.[10]

The spread of the φ and τ values characterizing the conformations of the different energy minima has been analyzed in a global way. Cumulating all six independent φ values to obtain just one average representative as well as averaging the three individual τ values found for each conformer through the minimization process to a mean value of this torsion, the distributions shown in Figure 12b/c are obtained. There are clear preferences at around 40° and 140° for the rotational positions of the aryl groups and, of course, by the very symmetry of the problem, at around −40° and −140° (Figure 12b). The spread of the τ values is more uniform with a slight preference for torsions of around 0° and ±30° (Figure 12c). If the rotational positions of the aryl groups are analyzed individually, pronounced regularities are observed.[22]

The distinct types of mutual orientation at each specific P(*o*Tol)$_2$ group have been systematically labelled using the scheme shown in Figure 13. To describe the aforementioned regularities, the orientations are classified according to the direction in which the two methyl groups are pointing. If, for the sake of definition, "inward" means that in the projection shown (Figure 13) the methyl group lies within the sector defined by the two P−C_{ipso} bonds and outward means that it lies outside, then three classes of arrangements may be defined. Firstly, for an arrangement where both methyl groups point inward, we use the term "syn" (Figure

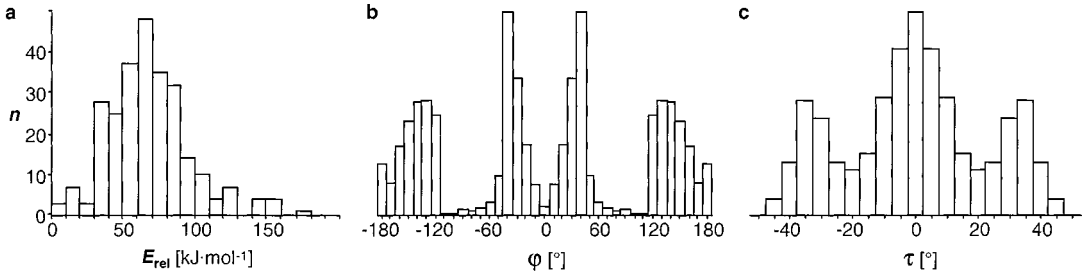

Figure 12. Histograms showing the distributions of the energies (a) and of the parameters φ (b) and τ (c) relating to the local minima found for compound **3**

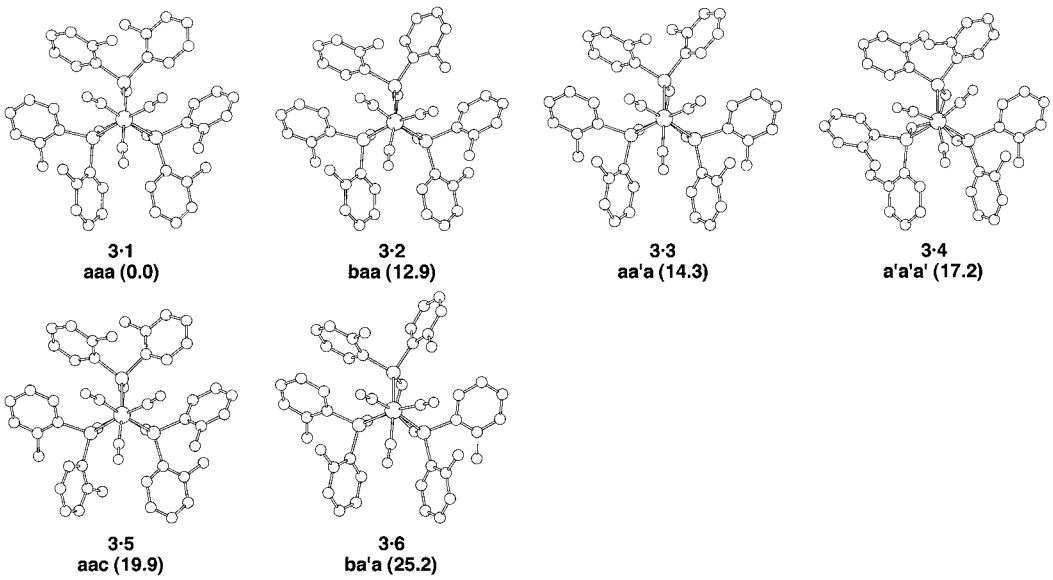

Figure 13. Conformations of **3** corresponding to local minima on the energetic hypersurface

13, 3.1). Secondly, where both methyl groups point outward, the arrangement shall be classified as "anti". The final arrangement, where one methyl group points inward and the other points outward, is referred to as "peri" (Figure 13, 3.2). For each class of orientation thus defined, there are further subclasses depending on whether a specific methyl group is on the left-hand or on the right-hand side and whether it points forwards or backwards. Designator *a* denotes a "syn" orientation with the left-hand *o*-tolyl group pointing forward and the right-hand one pointing backwards (Figure 13, 3.1). A "peri" arrangement of the methyl groups with both of them pointing forward is denoted as *b* (Figure 13, 3.2). Finally, a "peri" arrangement with both methyl groups pointing backwards is denoted as *c* (Figure 13, 3.5). These designators are combined to give the three-letter codes indicated in Figure 13, which describe the orientations adopted by the three P(*o*Tol)$_2$ groups in the sequence P1/P2/P3 (for the numbering scheme, see the definition in Figure 11). An orientation not shown in Figure 13, but referred to in Figure 14a and throughout the text, in which the left-hand methyl group points backwards and the right-hand one points forward while being in a mutual "anti" arrangement, is designated *d*.

For each of these local conformations, classified as *a*, *b*, *c*, or *d* as outlined above, an obverse conformation exists with forward and backward directions exchanged. These conformations are encoded by a prime (see, for instance, *a*′ in Figure 13, 3.4). The resulting eight designators suffice to characterize all the conformations up to calculated relative energies of around 60 kJ·mol^{-1}.

Analyzing the ensemble of conformers with respect to the specific classes to which their PAr$_2$ groups can be assigned, it is found that up to an energy of 27 kJ·mol^{-1} all these low-energy conformations have at least two local conformations

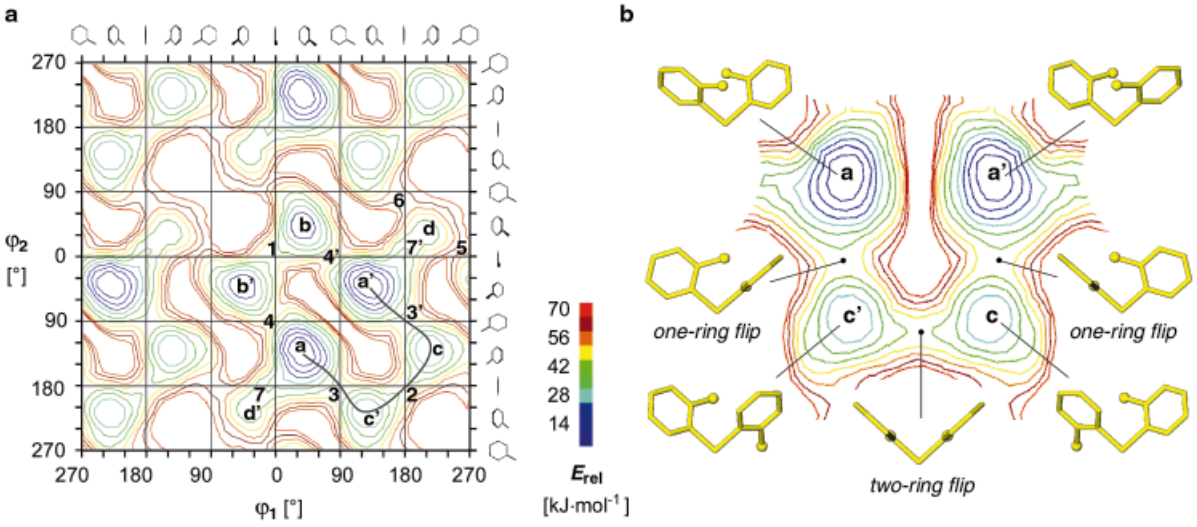

Figure 14. Contour diagram showing the enantiomerization pathway of **3**

corresponding to *a* or *a′* as defined above. This type of local orientation appears to be of peculiar stability.

The observation that conformations in which two of the P(*o*Tol)$_2$ groups remain in the orientation characterizing the arrangement of all three of these groups in the global minimum allows for a simplification of the conformational search. Selecting just one P(*o*Tol)$_2$ group and driving the rotational positions of its *o*-tolyl groups through the whole range of values from 0° to 360° should be sufficient to delineate the pathway of the overall isomerization process. The two remaining P(*o*Tol)$_2$ groups, which are not driven, will adopt the appropriate orientations during the minimization process. To allow for the torsional flexibility of the chelate scaffolding, these scans were made at two different settings of the torsion angle τ. To generate the starting conformations, all three torsion angles of one conformer were set at the same value and two complete scans of φ values were made, one at τ = 10° and the other at τ = 31°. These starting values were selected because analyses of similar compounds[8] have shown the τ values to cumulate around these values. The search was only performed with positive starting values of τ owing to the fact that all conformations must exist in isoenergetic enantiomeric pairs such that for every conformation with a given set of τ and φ values, an inverted conformation exists where the τ and φ values each have opposite signs. To allow for the torsional flexibility of the P(*o*-Tol)$_2$ groups that are not actively driven, the starting conformations of these groups were set according to the optimum arrangement (φ values) found to be characteristic for each value of τ. Initially, for small τ values an orientation as found for the global minimum (Figure 13, 3.1) was chosen, while for large τ values an orientation as shown in 3.4 (Figure 13) was used.

The subspace thus defined for the grid search has three dimensions; two aryl rotations φ_1 and φ_2 at the selected P(*o*Tol)$_2$ group and τ as a third dimension. While the τ space was only probed at two levels, the φ space was analyzed by a full rotation of both *o*-tolyl groups with an initial increment of 10°. To illustrate the result of these computations, a projection onto the subspace defined by the two aryl torsions φ_1 and φ_2 is shown in Figure 14.

Of the two energy values available at each grid point, resulting from the two values of τ assigned to it, the lower one was selected for this projection in each case. To generate the contour plot, we applied a symmetry expansion reflecting (i) the 360° translational symmetry along the φ axes, and (ii) the symmetry equivalence of enantiomeric pairs in each case. This second symmetry is evident from the diagram as a diagonal mirror plane from top left to bottom right (Figure 14).

There are three symmetrically independent energy minima apparent in this diagram. Position *a* (Figure 14; the designators *a*, *b*, *c*, *d* as used here are in accord with the definition given above in relation to Figure 13) corresponds to the global minimum. The minimum corresponding to the enantiomeric conformation is designated as *a′*. The local minima designated as *b*/*b′* correspond to an enantiomeric pair of conformations, as do the minima designated as *c*/*c′*. The positions *d*/*d′* correspond to another local minimum albeit a very flat one. The local minima *b*/*b′* (ca. 33 kJ·mol^{-1}) and *c*/*c′* (ca. 35 kJ·mol^{-1}) as well as the flat minimum *d*/*d′* (ca. 54 kJ·mol^{-1}) are all well above the energy of the global minimum *a*/*a′* (0.0 kJ·mol^{-1}). The diagram is thus consistent with the observation that only the enantiomeric conformations corresponding to the global minimum (*a*/*a′*) are seen in the NMR experiments. Although the local minima are relatively high in energy with respect to the equilibrium conformation *a*/*a′* and do thus not make a significant contribution to the conformational ensemble on thermodynamic grounds, the question still remains as to whether, once formed, they might survive due to the height of the relevant activation barriers. If this were to be the case, a thermodynamic equilibrium would not be established.

A rough estimate of the different activation barriers may be made simply by analyzing the diagram (Figure 14). The activation barriers associated with processes transforming *b′* back to *a* and *c′* back to *a* should be about 30 and 35 kJ·mol^{-1}, respectively, which are lower than those for the inverse processes, i.e. for transforming the conformation corresponding to the global minimum into the conformations characterizing the local minima *b′* and *c′*, respectively. A very rough estimate of the barriers associated with the latter transformations, as taken from the diagram, would be of the order of 50 kJ·mol^{-1} or higher. From these estimates of the relative energies of the activation barriers, it follows that the system as a whole should be in thermodynamic equilibrium under the conditions of the NMR experiments.

As far as the racemization process itself is concerned, only two plausible alternatives are suggested by the diagram: a trajectory along *a*−*b′*−*b*−*a′* or, alternatively, a transformation along *a*−*c′*−*c*−*a′*, which ever has the lower activation energy. By a more detailed analysis (see below), it is found that the latter pathway is in fact the important one.

The section of the diagram corresponding to this pathway is reproduced at the right-hand side of Figure 14 as an enlarged inset. Around this inset, the conformations characteristic of some selected points on the φ_1, φ_2 diagram are shown. It can be seen that following the pathway *a*−*c′*−*c*−*a′* corresponds to the transition of three saddle-points, which characterize one-ring, two-ring, and one-ring flip transitions in this sequence.[23]

In order to model the possible transformation pathways in a more accurate way, which would ultimately allow the extraction of reliable estimates of activation barriers, the following procedure was adopted. Starting with the ground state conformation, the P(*o*Tol)$_2$ group at P1 was selected for active rotation of its *o*-tolyl groups. A rotational increment of 2° was used throughout this analysis. The forward and backward rotations of these two *o*-tolyl groups have a different physical meaning due to the chirality of the system (this is even true at points in conformational space which, like the global minimum, correspond to C_3-symmetric arrangements).

To analyze the consequence of these rotations, each of these *o*-tolyl groups was actively driven and after each step the molecule as a whole was allowed to relax with the actively driven ring being fixed at the set position. It was found that − over a large range − the other *o*-tolyl group at P1 monotonically adopted its own rotational position in response to that of the driven group. Referring to the diagram in Figure 14, rotation of φ_1 in a negative direction, as well as independently starting with rotations of φ_2 in a positive direction, led to a route along the valley in the direction $a-b'$. Starting with φ_1 as the active rotator caused the system to follow the valley leading from *a* to *c'*. When the search was started by incrementing the rotation φ_1 in a negative sense, entry into a valley leading to *d'* was opened. Stepwise rotation in all four of these starting directions, with the appropriate relaxation after each step, led to the minima *b', c'*, and *d'* without further manipulation.

The saddlepoint 4 (Figure 14) was found at 79 kJ·mol^{-1}, irrespective, of course, of how it was arrived at. The saddlepoint 3 (Figure 14) connecting *a* and *c'* was found at 55.8 kJ·mol^{-1}, while that close to 7, separating *d'* from *a*, was found at 75 kJ·mol^{-1}.

With the analysis driven so far, a transformation following the direction *a* to *c'* is the most probable one and, as long as the saddlepoints separating *c'* from *c* and *c* from *a'* are lower in energy than the saddlepoints along the routes $a-b'$ or $a-d'$, this route is necessarily the best one. Accordingly, on driving φ_1 from its position at *c'* further in the positive direction, the local minimum *c* was reached without further interference. The saddlepoint between *c'* and *c* (2, Figure 14) was found at 52.1 kJ·mol^{-1}. If φ_1 was then further driven in a positive direction, a transition to the symmetry equivalent of *c'* was observed. Therefore, in order to delineate the route from *c* to *a'*, φ_2 was driven from this point on. In this way, *a'* was reached, the saddlepoint being found at 69.2 kJ·mol^{-1}. This is the maximum energy required for the conformational enantiomerization of the selected P(*o*Tol)$_2$ group along the route $a-c'-c-a'$. Since the saddlepoints separating *a* from *b'* as well as from *d'* are higher in energy, the routes via *b'* and *d'* do not need to be considered further.

The analysis described so far is not yet complete. There remain the other two P(*o*Tol)$_2$ groups, the rotational positions of which might, in principle, have a strong influence on the barrier height. During the optimization process described so far, the conformation at these groups remained essentially the same as in the starting conformation, with only minor undulations around the starting positions. On the one hand, this shows that coupling between neighboring P(*o*Tol)$_2$ groups is weak as compared to that dominating the interactions between two *o*-tolyl groups at one and the same phosphorus atom. Nevertheless, on the other hand, it has to be analyzed to ascertain whether any other rotational position of these neighboring P(*o*Tol)$_2$ groups would lead to a more favorable transition energy.

To simplify this problem, the following assumption was made. The lowest energy pathway for a rotational enantiomerization at each of these groups should be analogous to that already delineated for the group at P1. This assumption is well supported by the observation of almost decoupled behavior for the individual P(*o*Tol)$_2$ groups. To produce the analogous transitions, the rotations φ_3 (at P2) and φ_5 (at P3), respectively, were driven in a positive direction. This led directly to minima corresponding to *c'* with activation barriers of 73.6 kJ·mol^{-1} and 65.4 kJ·mol^{-1}. Due to the C_1 symmetry of the problem, the two routes are distinctly different and it is energetically more feasible to rotate the groups at P3 first. Driving φ_5 further in the positive direction led over a saddlepoint at 48.8 kJ·mol^{-1} to a minimum analogous to *c*. Driving φ_5 in the negative direction from this point on led to a minimum conformation locally enantiomeric to the starting conformation at P3 and thus analogous to *a'*. The saddlepoint for this last transition was found to be at 60.3 kJ·mol^{-1}. The same procedure was then applied to the rotation of the *o*-tolyl groups at P2. The saddlepoints in a sequence corresponding to the positions $a-c'-c-a'$ were found at 49.5, 44.7, and 43.6 kJ·mol^{-1}. Taking all the values together, it emerged that the energetically most costly step is the conformational enantiomerization of the first P(*o*Tol)$_2$ group (there is only one such "first" group due to the C_3 symmetry of the ground state conformation). Within the scope of the model, the value of 69.2 kJ·mol^{-1} (*mm2f*) or 61.1 kJ·mol^{-1} (*mm2t*) thus characterizes the activation energy for the racemization of the compound. The sequence of individual rotations taking place over the whole process is illustrated in Figure 15, which shows the conformations of all the minima encountered along this route.

The labels *a*,*a'* and *c*,*c'* correspond to the labels in Figure 13. The three-letter code refers to the local conformation at the phosphorus atoms P1, P2, and P3 in this sequence. The relative energies, together with the values quantifying the conformations, are given in Table 2, as are the energies calculated for the intervening saddlepoints. The energy profile given in Figure 16 summarizes the energetics of the pathway in a condensed form.

Analysis of 2

The structure of **2** is not known from crystallography. In order to model the low-energy structures, it was − in view of the knowledge already acquired with compounds of this type[12] − not considered necessary to carry out a full conformational search. Starting conformations, which should be close to the global minimum, were constructed either from low-energy conformations of $CH_3C(CH_2PPh_2)_3Mo(CO)_3$ by adding methyl groups at the appropriate positions to transform the phenyl groups into *o*-tolyl groups, or from low-energy conformations of $CH_3C[CH_2P(oTol)_2]_3Mo(CO)_3$ (**3**) by the reverse operation. Starting conformations with both types of helicity with respect to the arrangement of the aryl groups and with high (ca. 30°) and low (ca. 10°) values of the torsional arrangement of the chelate cage were analyzed. Refinement of all these conformations led to two analogous minima in each case. A con-

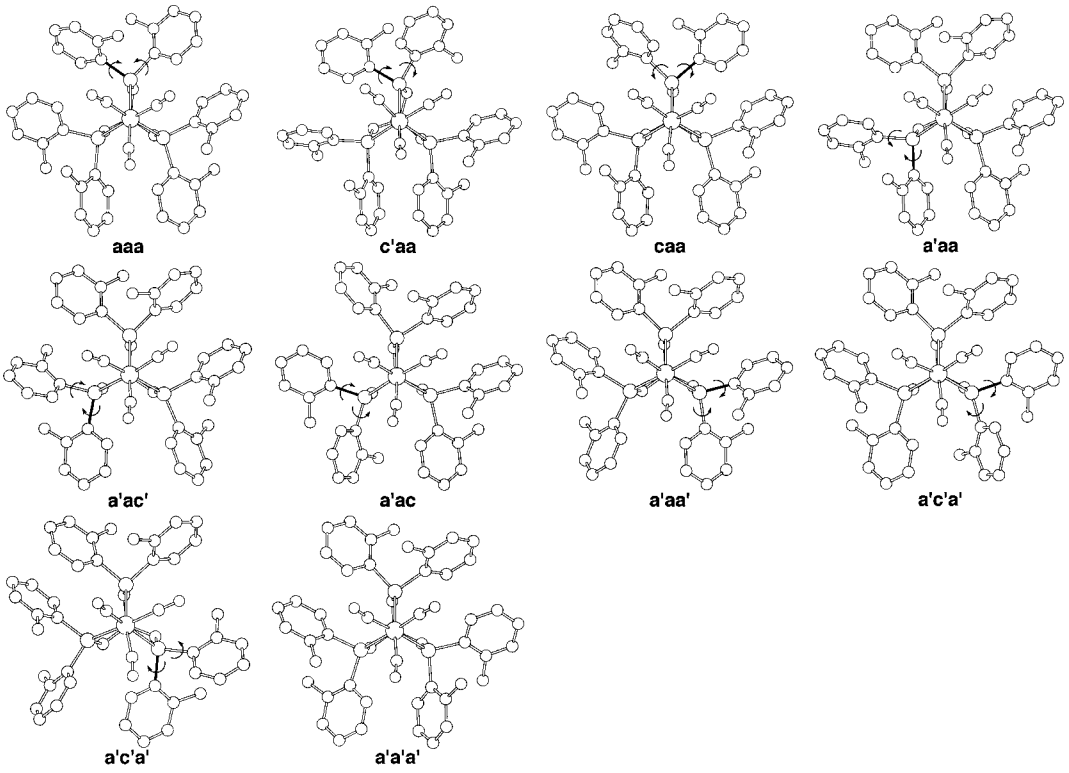

Figure 15. Sequence of rotational processes along the enantiomerization pathway of **3**

Table 2. Conformations of **3** characterized by their φ and τ values (*mm2f* parameter set)

i	*ring flip*	E_{rel}(TS) [kJ·mol^{-1}]	E_{rel} [kJ·mol^{-1}]	Codon[a] P1P2P3	φ_1 [°]	φ_2 [°]	φ_3 [°]	φ_4 [°]	φ_5 [°]	φ_6 [°]	τ_1 [°]	τ_2 [°]	τ_3 [°]
–	–	–	0.0	**aaa**	34	–127	34	–127	34	–127	10	10	10
1	1-r. f.	55.8	35.1	**c'aa**	118	128	33	–141	23	–160	27	10	31
1	2-r. f.	52.1	19.9	**caa**	–146	–127	34	–128	36	–125	5	6	3
2	1-r. f.	**69.2**	14.3	**a'aa**	123	–37	34	–130	32	–148	9	6	19
5	1-r. f.	**65.4**	38.9	**a'ac'**	128	–32	33	–143	125	147	5	9	–2
5	2-r. f.	48.8	38.9	**a'ac**	143	–33	32	–128	–147	–125	–9	–5	2
6	1-r. f.	60.3	14.3	**a'aa'**	130	–34	37	–123	148	–32	–6	–9	–19
3	1-r. f.	**59.5**	19.9	**a'c'a'**	128	–34	127	146	125	–36	–6	–5	–3
3	2-r. f.	54.7	35.1	**a'ca'**	141	–33	–128	–118	160	–23	–10	–27	–31
4	1-r. f.	43.6	0.0	**a'a'a'**	127	–34	127	–34	127	–34	–10	–10	–10

[a] For the meaning of the designators, see the text and Figure 15.

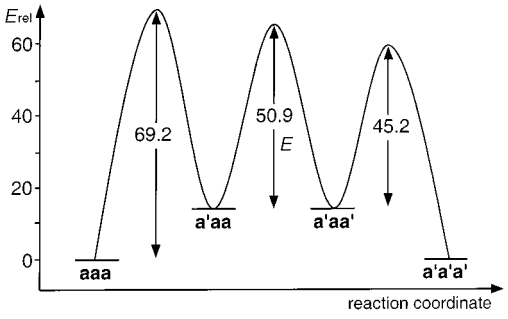

Figure 16. Energy profile along the enantiomerization pathway of **3**; E_{rel} in kJ·mol^{-1}; for the meaning of the designators, see Figure 15

formation with small τ values (Table 3) was found as the global minimum (this is shown as 2*sf* in Figure 17).

Table 3. Energies and conformational parameters of the two pairs of low-energy conformations of **1** and **2** for the parameter sets *mm2f* and *mm2t* (designators refer to Figure 17)

	Parameter	E_{rel} [kJ·mol^{-1}]	φ_1 [°]	φ_2 [°]	φ_3 [°]	φ_4 [°]	φ_5 [°]	φ_6 [°]	τ_1 [°]	τ_2 [°]	τ_3 [°]
1*sf*	*mm2f*	0.0	38	–135	35	50	37	49	7	11	9
1*st*	*mm2t*	8.8	29	–126	29	57	27	59	18	19	20
1*lf*	*mm2f*	2.1	118	–38	–36	–20	–48	–27	27	33	36
1*lt*	*mm2t*	0.0	118	–41	1	–14	–47	–29	29	36	39
2*sf*	*mm2f*	0.0	40	–135	38	–136	35	50	6	8	10
2*st*	*mm2t*	5.6	30	–126	30	–125	29	58	17	17	19
2*lf*	*mm2f*	5.9	120	–40	122	–38	–31	–21	29	23	35
2*lt*	*mm2t*	0.0	120	–39	121	–38	–3	–18	34	26	39

A conformation with relatively large τ values is only around 6 kJ·mol^{-1} higher in energy (Figure 17, *2lf*). It is predicted that one of these conformations (as quantified in Table 3) would be found if the structure of **2** were to be accessible to X-ray crystallography. This result was obtained using the *mm2f* parameter set.[10] On applying the *mm2t*[10] parameter set, qualitatively identical conformations were obtained (Figure 17, 2*st*, 2*lt*). With the force field approach *mm2t*, the conformation with the large values for the torsion angles of the cage was found at the absolute minimum, while the other one, corresponding to small cage torsions τ, was calculated to lie 6 kJ·mol^{-1} above it. The relative energies of the two lowest-energy conformations of **2**, as calculated by the two parameter sets, are

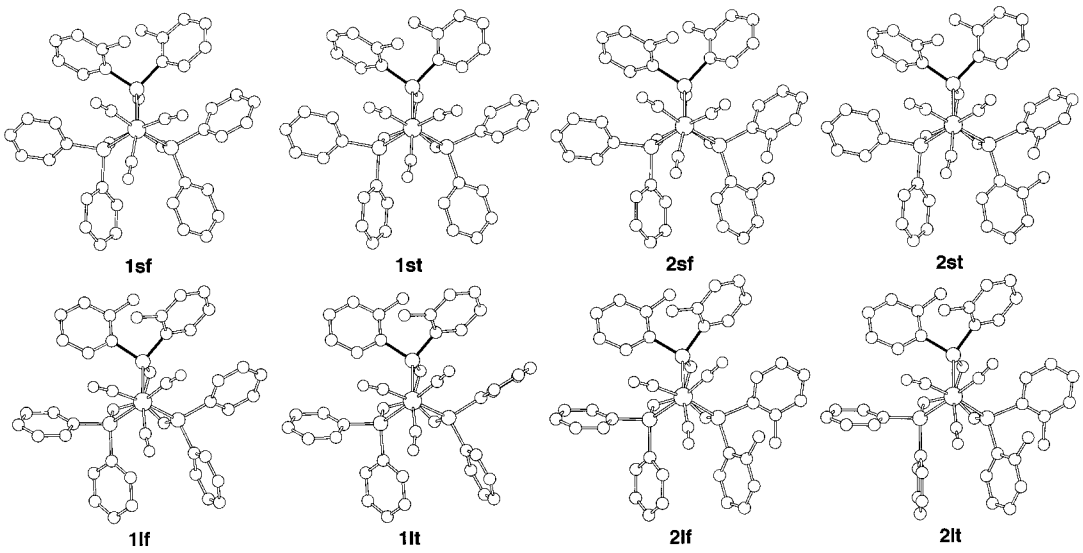

Figure 17. Lowest-energy conformations of **1** and **2** as calculated with the force field parameter sets *mm2f* and *mm2t*; the extensions *f* and *t* are used to designate the force field parameter set *mm2f* and *mm2t*, while the designators *s* and *l* refer to small and large torsions of the chelate cage

given in Table 3, together with the values quantifying these conformations.

Analysis of the racemization of the conformation corresponding to the global minimum was carried out in a similar manner as described in detail for compound **3**. The contour diagram obtained for the rotational inversion of the first P(*o*Tol)$_2$ group is very similar to that shown for **3** in Figure 14. The same types of minima and saddlepoints are observed. The energetic differentiation is, however, less pronounced than in the case of **3**. In the case of **2**, it is of relevance which of the two P(*o*Tol)$_2$ groups is selected as the first one to be subjected to the forced rotation process. Once one P(*o*Tol)$_2$ group is selected, its neighboring PAr$_2$ groups are no longer equivalent. The PPh$_2$ group is either on the left-hand or on the right-hand side of the selected fragment. This situation is reflected in the contour plot, which is no longer strictly symmetrical with respect to an idealized mirror plane lying along the diagonal.

The least-energy pathway from the global minimum coded as *aaa* in Figure 18 to its enantiomer *a′a′a′* traverses the local minima shown in Figure 18, where the meaning of the three-letter code is the same as that used for the description of **3**; due to the C_2 symmetry of the phenyl groups, only the two designators *a* and *a′* are necessary to describe the arrangement of the PPh$_2$ groups.

There is no need to actively rotate the phenyl groups; they are found to automatically orientate themselves during the minimization processes. Their reorientation is characterized by a two-ring flip transition (Figure 18, *aca*−*aa′a*). The relative energies of the corresponding minima, together with their corresponding conformational parameters and the energies of the saddlepoints en route from *aaa* to *a′a′a′* according to Figure 18, are given in Table 4.

The assignment of the individual transition processes in terms of one-ring and two-ring flip transitions given in Table 4 is also apparent from Figure 18. It is found that the highest barrier is associated with inversion of the second P(*o*Tol)$_2$ group; a barrier height of 56.5 kJ·mol^{-1} (*mm2f*) or 57.1 kJ·mol^{-1} (*mm2t*) is calculated for this step, which, within the model, characterizes the activation barrier.

Analysis of 1

The structure of **1** is not known experimentally. The low-energy conformations for **1** were calculated on a similar basis as discussed above in the case of **2**. Irrespective of the starting geometries, which were also refined as discussed for **2**, two low-energy conformations were found (*mm2f* [10]), energetically very close together (2.1 kJ·mol^{-1}) and structurally differentiated in the same way as described for **2**. These conformations were also found with *mm2t* as the force field, albeit with interchanged relative energies.

One of the calculated low-energy conformations of **1** has small torsions τ of the chelate cage and a left helical arrangement of the aryl groups (Figure 17, 1*sf*, 1*st*; Table 3). The other one has large τ values with the helicity of the aryl "propeller" being, in principle, right-handed (Figure 17, 1*lf*, 1*lt*; Table 3). The contour plot for the local enantiomerization of the P(*o*Tol)$_2$ group is again qualitatively similar to that shown for **3** and is of course symmetrical due to the mirror plane along the diagonal of this type of diagram. The calculated energies are somewhat lower than those obtained for **2**, which are in turn lower than those calculated for **3**. This is a consequence of the decreasing steric strain on descending the sequence **3**, **2**, **1**. Detailed analysis of the racemization pathway was performed as extensively as described for **3**. In contrast to the observations made for **2**, the phenyl groups do not completely adapt to the rearrangement at the P(*o*Tol)$_2$ group and have hence to be actively driven in the final step. The lowest-energy pathway for the racemization of **1** is qualitatively analogous to those described for **3** and **2**.

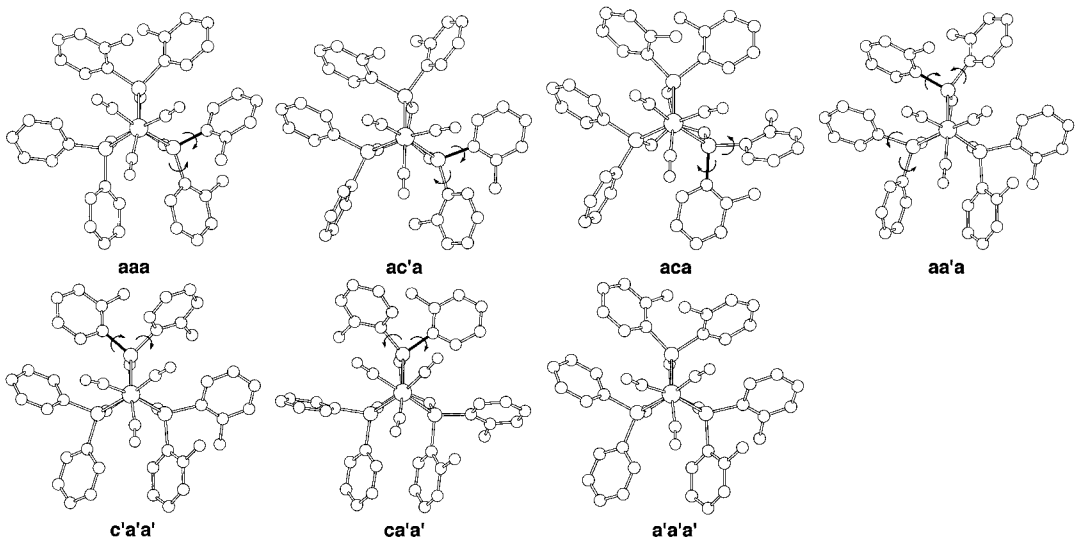

Figure 18. Sequence of rotational processes along the enantiomerization pathway of **2**

Table 4. Conformations of **2** characterized by their φ and τ values (*mm2f* parameter set)

i	*ring flip*	E_{rel}(TS) [kJ·mol^{-1}]	E_{rel} [kJ·mol^{-1}]	Codon[a] P1P2P3	φ_1 [°]	φ_2 [°]	φ_3 [°]	φ_4 [°]	φ_5 [°]	φ_6 [°]	τ_1 [°]	τ_2 [°]	τ_3 [°]
–	–	–	0.0	**aaa**	40	–135	38	–136	35	50	6	8	10
3	1-r. f.	53.8	28.5	**ac'a**	28	–154	118	130	10	32	24	12	2
3	2-r. f.	50.4	24.1	**aca**	36	121	–148	–117	15	25	–22	–30	–36
4	1-r. f.	50.3	11.4	**aa'a**	33	–143	124	–36	24	41	14	2	0
1	1-r. f.	**56.5**	21.7	**c'a'a'**	126	145	125	–37	–45	–36	–5	–3	–7
1	2-r. f.	51.3	28.5	**ca'a'**	–130	–118	154	–28	–32	–10	–12	–24	2
2	1-r. f.	52.5	0.0	**a'a'a'**	136	–38	135	–40	–50	–35	–8	–6	–10

[a] For the meaning of the designators, see the text and Figure 18.

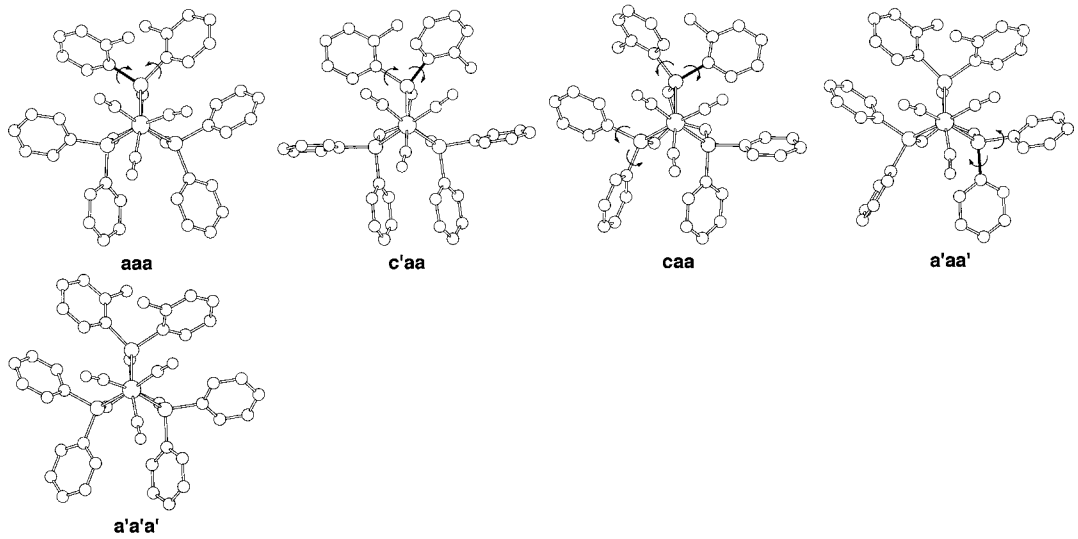

Figure 19. Sequence of rotational processes along the enantiomerization pathway of **1**

Figure 19 illustrates the local minima encountered along this pathway. The energies of these minima, together with those of the saddlepoints separating them, are given in Table 5. The highest barrier dominating the process as a whole is found at 53.1 kJ·mol^{-1} (*mm2f*) or 44.0 kJ·mol^{-1} (*mm2t*).

Table 5. Conformations of **1** characterized by their φ and τ values (*mm2f* parameter set)

i	*ring flip*	E_{rel}(TS) [kJ·mol^{-1}]	E_{rel} [kJ·mol^{-1}]	Codon[a] P1P2P3	φ_1 [°]	φ_2 [°]	φ_3 [°]	φ_4 [°]	φ_5 [°]	φ_6 [°]	τ_1 [°]	τ_2 [°]	τ_3 [°]
–	–	–	0.0	**aaa**	38	–135	35	50	37	49	7	11	9
1	1-r. f.	42.0	22.2	**c'aa**	116	128	9	27	20	6	16	3	27
2	2-r. f.	**53.1**	22.3	**caa**	–150	–116	21	42	19	41	–28	–37	–30
2	1-r. f.	42.9	3.4	**aaa'**	138	–36	30	64	–5	–21	–11	–18	–27
4	1-r. f.	9.6	0.0	**a'a'a'**	135	–38	–49	–37	–50	–35	–7	–9	–11

[a] For the meaning of the designators, see the text and Figure 19.

Table 6. Comparison between calculated and measured activation barriers for **1**–**3**

Compound	ΔH_{calc} [kJ·mol^{-1}] *mm2f*	ΔH_{calc} [kJ·mol^{-1}] *mm2t*	$\Delta G^{\neq}_{298K}$ [kJ·mol^{-1}] NMR	$\Delta H^{\neq}$ [kJ·mol^{-1}] NMR	$\Delta S^{\neq}$ [J·K^{-1}·mol^{-1}] NMR
1	53.1	44.0	54.3	45.3	–30
2	56.5	57.1	57.9	51.8	–20
3	69.2	61.1	65.5	59.3	–21

Comparison of Calculated and Measured Activation Barriers

Comparison of the calculated activation barriers with those observed for **1**–**3** provides a means of assessing the quality of the force field approach and especially of assessing the appropriateness of the energy scale produced by the force field approach.[24] It has previously been shown that the force field approach used is capable of correctly reproducing NOE distances in a series of compounds.[12] The best one can do in this respect is to use the energies calculated by the force field as the basis to produce a Boltzmann weighted average. Even though $\Delta G^{\neq}$ values would be necessary to make this approach a physically correct one, $\Delta H^{\neq}$ values, as obtained by the force field approach, are still the best and only choice one has. The fact that the NOE distances calculated by this approach are in close agreement with the observed values indicates that the calculated $\Delta H^{\neq}$ values are somehow on scale with the $\Delta G^{\neq}$ values.[12]

The results obtained for the activation energies of **1**–**3** using the force field approach appear highly satisfying in this respect (Table 6). Irrespective of the type of force field used (*mm2f*, *mm2t*), the activation energies are predicted to increase with increasing steric congestion on ascending the series **1**, **2**, **3**. The energies given by the force field approach do not contain entropy terms and thus have to be compared with the $\Delta H^{\neq}$ values as the experimental counterpart. Using the *mm2f* parameter set, the predicted energies are equal to the experimental values with a maximum deviation of 10 kJ·mol^{-1}; based on the *mm2t* set of parameters, the maximum deviation is only around 5 kJ·mol^{-1} (Table 6). With either parameter set, the ranking of the compounds in order of increasing activation barriers is correctly predicted. Indeed, the agreement between calculated and experimental values is as good as might be hoped for using a force field approach. This may be taken as a further confirmation of the validity of the approach taken to derive the force field parameters.

Conclusion

1. *Tripod* compounds $CH_3C(CH_2PPh_2)_{3-n}[CH_2P(o\text{-}Tol)_2]_nMo(CO)_3$ ($n = 1-3$) undergo conformational enantiomerization with activation barriers $\Delta H^{\neq}$ between 45 and 59 kJ·mol^{-1}. The barriers increase with increasing number of P(oTol)$_2$ groups present.

2. Using a force field approach, for which the force field parameters were derived by global optimization on the basis of all the structural information available,[10] reaction pathways for these enantiomerization processes have been delineated. The activation barriers predicted by this approach are in close agreement with the experimental values.

3. The approach of deriving force field parameters by global optimization over a complete basis of molecular structures[10][11] is capable of predicting conformations and conformational energy differences in agreement with experimental findings.

Experimental Section

General Remarks: All manipulations were carried out under an argon atmosphere at 20°C by means of standard Schlenk techniques, unless mentioned otherwise. All solvents were dried by standard methods and distilled under argon. The solvents used for the NMR spectroscopic measurements were degassed by three successive "freeze-pump-thaw" cycles and were dried over 4 Å molecular sieves. The silica gel (Kieselgel p.A. 0.06–0.02 mm, J. T. Baker Chemical B.V.) used for chromatography and the Kieselgur (Kieselgur, washed, heat-treated, Erg. B.6, Riedel de Haen AG) used for filtration were degassed at 1 mbar at 20°C for 48 h and then saturated with argon. – IR: Bruker FT-IR IFS-66; CaF_2 cells. – MS(EI): Finnigan MAT 8400. – Elemental analysis: Microanalytical laboratory of the Organisch-Chemisches Institut, Universität Heidelberg. Under the conditions employed, the carbon content is often found to be too low for molybdenum-containing compounds due to the formation of non-combustible molybdenum carbide. – Melting points: Gallenkamp MFB-595 010; uncorrected values. – All chemicals were obtained commercially and were used without further purification.

NMR: NMR spectra were recorded on Bruker NMR spectrometers operating at 200, 300, and 500 MHz, respectively. Two-dimensional spectra were recorded with quadrature detection in both dimensions; TPPI was used in F_1. All information about sizes and data points of the spectra is given in real points. ^{1}H- and ^{13}C-NMR spectra were calibrated internally using the residual solvent signals (CD_2Cl_2, $\delta_H = 5.32$, $\delta_C = 53.8$; $CDCl_3$, $\delta_H = 7.24$, $\delta_C = 77.0$) and tetramethylsilane (TMS, $\delta = 0$) as an external standard; ^{31}P-NMR chemical shifts are given in ppm relative to 85% H_3PO_4 ($\delta = 0$) as an external standard. Assignment of all the ^{1}H, ^{13}C, and ^{31}P resonances was accomplished by a combination of 1D and 2D NMR experiments (DQF-COSY,[13] TOCSY,[14] NOESY,[15] {^{1}H-^{13}C}-HSQC,[16] {^{1}H-^{13}C}-HMBC,[17] {^{1}H-^{31}P}-HMBC;[17] see Tables 12−14, Figure 20). For NMR analysis, saturated solutions of the compounds in CD_2Cl_2 (**1**, **2**) and $CDCl_3$ (**3**) were prepared in precision NMR tubes on a vacuum line; the tubes were flame-sealed after deoxygenation by repeated evacuation followed by readmission of argon (minimum of three freeze/pump/thaw cycles). The experimental set-ups for the various experiments are outlined in Tables 7 and 8. While compounds **1** and **2** were analyzed by a combination of all the available methods (Table 7), analysis of **3** had to be limited to a subset of these methods as indicated in Table 8.

The temperature was calibrated using a [D_4]methanol (99.8%) NMR thermometer[25] in the low-temperature range (−100°C to 30°C) and ethylene glycol at higher temperatures (20−180°C).[26] Temperatures were kept constant to within ±0.2 K (DRX500) and ±1 K (DRX300, DPX200, AC200). As judged from the calibration with [D_4]methanol, the actual sample temperatures were accurate to within approximately ±1 K. Various parameters relating to the equipment used and the experimental set-ups are given in Tables 9−11, while ^{31}P-NMR data of **1**−**3** are given in Table 12.

A matrix representation of the different types of cross-correlation signals observed for **3** is presented in Figure 20.

Tables 13 and 14 show ^{13}C- and ^{1}H-NMR data of **1** and **2**, together with the correlations used for assignment and analysis.

Experiments and Analyses: The assignments were made according to standard procedures, the salient details of which are given in Tables 12−14 and Figure 20. Rate constants were estimated using three different approaches, the most straightforward of these involving determination of the coalescence temperature. This type of experiment was performed at different field strengths and by using both ^{1}H- and ^{31}P-NMR spectroscopy (Tables 1 and 10). A somewhat more extended range of temperatures was covered by EXSY experiments based on exchange signals between pairs of different types of protons; these were also performed at different field strengths (Tables 1 and 11). The most extensive range of temperatures was covered by line-shape analysis of the ^{31}P-NMR signals. This type of experiment was, of course, limited to compounds **1** and **2** owing to the constitutional C_3 symmetry of **3**. Again, different field strengths were used for these experiments (Tables 1, 10, and 12). The quality of fit obtained is exemplified by the case of **2** in Figure 10. All the rate constants for **1** and **2** obtained by line-shape analysis were used to construct an Eyring plot in each case. Considering the error statistics, the enthalpy and entropy values obtained by this procedure would seem to be quite accurate (**1:** $R^2 = 0.998$, $\Delta H^{\neq} = 45.3 \pm 0.4$ kJ·mol^{-1}, $\Delta S^{\neq} = -30 \pm 1$ J·K^{-1}·mol^{-1}; **2:** $R^2 = 0.995$, $\Delta H^{\neq} = 51.8 \pm 0.7$ kJ·mol^{-1}, $\Delta S^{\neq} =$

Table 8. Set-up for 2D NMR experiments on **3**

	2D NMR experiment		
	DQF-COSY	TOCSY	NOESY
Pulse program[a]	cosyphdq.au	mlev17ph.au	noesyph.au
Temperature [K]	259	259	259
Instrument	AC200	AC200	AC200
Spectral width F_2 [Hz]	1639.34	1639.34	1639.34
Time domain F_2 [Word]	2 K	2 K	2 K
Size F_2 [Word]	2 K	2 K	2 K
Spectral width F_1 [Hz]	1639.34	1639.34	1639.34
Time domain F_1 [Word]	256	128	256
Size F_1 [Word]	512	512	1 K
Scans	32	48	48
Mixing time [ms]	-	170	400
Relaxation delay [s]	1.5	1.0	2.0

[a] The acronyms in this row refer to pulse sequences supplied under these names for the Bruker series of instruments.

Table 9. Equipment used for the DNMR experiments

Spectrometer	Temperature control unit	Cooling	NMR frequency [MHz]		
			^{1}H	^{31}P	^{13}C
DRX500	BVT3000	N_2 evaporator	500.130	202.456	125.758
DRX300	BVT3300	N_2 exchanger	300.130	121.495	75.468
DPX200	BVT3300	N_2 exchanger	200.130	81.014	50.323
AC200	BVT1000	N_2 evaporator	200.130	81.026	50.330

Table 7. Set-up for 2D NMR experiments on **1** and **2**

	2D NMR experiment											
	{^{1}H–^{13}C}-HSQC		{^{1}H–^{13}C}-HMBC		{^{1}H–^{31}P}-HMBC		DQF-COSY		TOCSY		NOESY	
Pulse program[a]	invigstp		inv4gslplrnd		inv4gslrnd		cosyphdq.au		mlev17ph.au		noesytp	
Compound	**1**	**2**	**1**	**2**	**1**	**2**	**1**	**2**	**1**	**2**	**1**	**2**
Temperature [K]	212	224	212	224	212	224	211	219	211	219	226	224
Instrument	DRX500	DRX300	DRX500	DRX300	DRX500	DRX300	AC200	AC200	AC200	AC200	DRX500	DRX500
Spectral width F2 [Hz]	3360.22	2042.48	3443.53	2069.54	3443.53	2069.54	1582.28	1683.50	1582.28	1683.50	3501.40	3415.30
Time domain F2 [Word]	4 K	2 K	4 K	2 K	4 K	4 K	2 K	2 K	2 K	2 K	1 K	4 K
Size F2 [Word]	2 K	2 K	2 K	1 K	2 K	2 K	4 K	4 K	2 K	2 K	1 K	2 K
Spectral width F1 [Hz]	2389.72[b]	4981.47[b]	16349.80	9811.69	1720.88	1032.71	1582.28	1683.50	1582.28	1683.50	3501.40	3415.30
Time domain F1 [Word]	256	256	512	512	128	128	512	256	256	256	128	128
Size F1 [Word]	1 K	1 K	1 K	1 K	1 K	1 K	1 K	1 K	512	1 K	1 K	1 K
Scans	32	38	30	24	24	24	32	48	32	48	32	24
Mixing time [ms]	-	-	70	50	60	60	-	-	125	200	600	200
Relaxation delay [s]	1.5	2.0	1.5	1.5	1.5	1.5	1.4	1.6	1.5	1.8	1.8	2.0

[a] The acronyms in this row refer to pulse sequences supplied under these names for the Bruker series of instruments. − [b] Folded in F1 dimension.

Table 10. Set-up for variable-temperature 1D NMR experiments on **1**−**3**

Compound	^{1}H NMR frequency	Temperature range [K] static[a]		dynamic[b]			^{31}P{^{1}H} NMR spectra[c]			^{1}H NMR spectra[c]		
							Spectral width	Time domain	Scans	Spectral width	Time domain	Scans
	[MHz]	T	(n)	T	(n)	[ΔT]	[Hz]	[Word]		[Hz]	[Word]	
1	500	206–226	(3)	270–300	(6)	[3/5/10]	10162.6	32 K	200	3472.2	32 K	16
	300	203–224	(3)	263–293	(5)	[5/10]	3655.0	16 K	200	2083.3	16 K	16
	200	165–206	(5)	216–313	(16)	[3/5/10]	2435.7	8 K	200	1436.8	16 K	16
2	500	206–241	(5)	270–307	(9)	[3/5]	10162.6	32 K	200	3472.2	32 K	16
	300	198–224	(4)	234–322	(14)	[5/10]	3655.0	16 K	200	2097.3	16 K	16
	200	221–253	(4)	258–304	(9)	[3/5/10]	5668.9	16 K	200	1398.2	16 K	16
3	200	158–261	(6)	278–343	(6)	[10]	8928.6	16 K	750	1639.4	32 K	64

[a] The number of spectra taken in the specified temperature range at intervals of ≈10 K is given in brackets (*n*). − [b] The number of spectra taken in the specified temperature range is given in brackets (*n*); square brackets: temperature increments used [Δ*T*]. − [c] A relaxation delay of 2 s was used throughout.

Table 11. Set-up for EXSY experiments on **1**−**3**

	Compound								
	1			**2**			**3**		
Frequency [MHz]	500	300	200	500	300	200	200	200	200
Temperature [K]	226.4	211.7	221.1	223.9	218.4	226.9	296.6	268.2	261.4
Spectral width F_1/F_2 [Hz]	3501.4	2042.5	1398.2	3415.3	2042.5	1388.9	1639.3	1639.3	1639.3
Time domain F_2 [Word]	1 K	2 K	1 K	4 K	2 K	2 K	2 K	2 K	2 K
Size F_2 [Word]	1 K	1 K	1 K	2 K	1 K	1 K	2 K	2 K	2 K
Time domain F_1 [Word]	128	128	128	128	128	128	256	256	256
Size F_1 [Word]	1 K	1 K	1 K	1 K	1 K	1 K	1 K	1 K	1 K
Scans	32	24	32	24	32	24	32	32	48
Mixing time [ms]	100/600	100–200[a]	10–300[b]	200	75/200	200	100	200	400
Relaxation Delay [s]	1.8	2.0	1.7	2.0	1.6	1.8	1.8	1.5	2.0

[a] 3 spectra were taken with mixing times of 100, 150, and 200 ms. − [b] 6 spectra were taken with mixing times of 10, 20, 50, 100, 200, and 300 ms.

-20 ± 2 J·K^{-1}·mol^{-1}; the limits given refer to the estimated standard deviation σ in each case; Table 1). Since ^{31}P-NMR line-shape analysis was not possible for **3**, the basis for estimating activation parameters was inferred from coalescence and EXSY data (Tables 1, 10, and 11). With only six available data points (Table 1), the statistical accuracy of the estimated parameter values is somewhat lower than those obtained for **1** and **2** on the basis of the data obtained by line-shape analysis (**3**: $R^2 = 0.986$, $\Delta H^{\neq} = 59.3 \pm 3.5$ kJ·mol^{-1}, $\Delta S^{\neq} = -21 \pm 12$ J·K^{-1}·mol^{-1}; limits refer to σ; Table 1). In order to get some appraisal of the mutual agreement between the data obtained by the three different techniques, the complete set of data obtained for **1** and **2**, irrespective of the acquisition procedure (line-shape analysis, EXSY spectroscopy, coalescence measurements) was also used to construct Eyring plots. Based on the complete set of data, $\Delta H^{\neq}$ and $\Delta S^{\neq}$ as estimated for **1** ($R^2 = 0.995$, $\Delta H^{\neq} = 45.7 \pm 0.5$ kJ·mol^{-1}, $\Delta S^{\neq} = -29 \pm 2$ J·K^{-1}·mol^{-1}; limits refer to σ; Table 1) are in excellent agreement with the values obtained from line-shape analysis alone (see above, Table 1). Apply-

Table 12. ^{31}P-NMR data for compounds **1**−**3**

Compound	*T* [K]	δ(P1)	δ(P2)	δ(P3)	$^2J_{P1P2}$ [Hz]	$^2J_{P1P3}$ [Hz]	$^2J_{P2P3}$ [Hz]
1	313[a]	21.91 t	—— 16.40 d ——		—— 22.79 ——		
	205	20.75 dd	16.15 dd	13.91 dd	29.04	17.76	25.04
2	322[a]	—— 21.79 d ——		16.06 t		—— 22.73 ——	
	198	19.67 dd	20.37 dd	13.99 dd	23.09	29.07	18.27
3	343	20.79 s					
	210	18.40 s					

[a] High-temperature limit, coalescence of **1**: P2/P3, **2**: P1/P2.

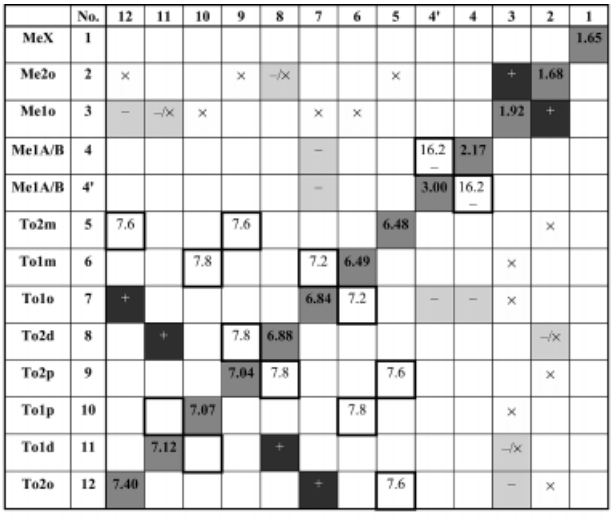

Figure 20. Matrix-type representation of the ^{1}H-NMR data of **3**; the meanings of the designators are as described for Figure 4; along the diagonal: chemical shifts; off-diagonal: H−H coupling constants (numbers); DQF-COSY cross-peaks bold framed, TOCSY cross-peaks (×), NOE cross-peaks light grey (−), EXSY cross-peaks dark grey (+); the data refer to a solution of **3** in $CDCl_3$ at 261 K (due to the low solubility and with the available equipment, exact ^{13}C-NMR data of **3** could not be obtained).

Table 13. ^{1}H- and ^{13}C{^{1}H}-NMR data of **2**; the meaning of symbols is as in Figure 3

	NMR Spectra			Correlations			Data for quaternary carbons		
No	Nucleus[a]	δ(^{13}C)[b]	δ(^{1}H)[c]	NOESY	EXSY	HMBC	No	Nucleus[a]	δ(^{13}C)[b]
1	**MeX**	40.13 q (9.6)	1.51 bs	Me1/2/3A/B		6/7/8/30	**30**	**Npq**	37.50 q (7.2)
2	**Me4o**	21.35[d] d (~2)	1.58 s	To4d/To3o/Me2B	Me1o	2/14/11//3238			
3	**Me2o**	21.22[d] d (~2)	1.70 s	Me1B/A/To2d		3/8/12/31/37	**31**	**Me2o$_{ipso}$**	132.10 dd (26.7/3.2)
4	**Me3o**	21.81[e] d (8.9)	1.74 s	To3d		4/9/10/15/34/39			
5	**Me1o**	21.58[e] d (9.5)	2.04 s	To1d/To2o	Me4o	5/13/21/33/40	**32**	**Me4o$_{ipso}$**	133.98 dd (27.1/4.4)
6'	**Me3B**	31.02 m (~10)	2.05 dd (16.0)[f]	Ph6o/Ph5o	Me3A	7/8/30//3536			
7'	**Me2B**	35.62 m (~10)	2.25 dd (15.6)[f]	Me4o/Me2A	Me1A	1/6/30/32	**33**	**Me1o$_{ipso}$**	134.06 dd (29.3/4.6)
8'	**Me1B**	34.33 m (~10)	2.41 dd (15.3)[f]	Me2o	Me2A	1/7/30/31			
8	**Me1A**	34.33 m (~10)	2.48 dd (15.3)[f]	Me2o/To1o/Ph6o	Me2B	6/7/30/31/33	**34**	**Me3o$_{ipso}$**	134.58 dd (32.8/4.7)
6	**Me3A**	31.02 m (~10)	2.64 dd (16.0)[f]	Ph5o/m/Me3B	Me3B	1/8/30/35			
7	**Me2A**	35.62 m (~10)	2.73 dd (15.6)[f]	To3o/Me2B	Me1B	6/8/30/32/34	**35**	**Ph5$_{ipso}$**	138.76 dd (26.5/5.9)
8	**To2m**	124.20 d (16.4)	6.11 pt (7.8/7.4)		To3m	3/12/16/29/31/37			
9	**To3o**	126.49 d (4.3)	6.22 pt (7.2)[f]	Me2A/Me4o	To2o	4/17/39	**36**	**Ph6$_{ipso}$**	139.88 d (2.9)
10	**To3m**	124.46 d (6.0)	6.41 pt (7.1/7.8)		To2m	9/15/17/34/39			
11	**To4m**	125.42 d (16.3)	6.60 pt (7.8/7.5)		To1m	2/14/20/28/32/38	**37**	**To2$_{ipso}$**	139.89 dd (32.5/5.9)
12	**To2d**	131.74 d (3.7)	6.86 d (7.6)	Me2o		3/8/31/37			
13	**To1m**	124.55 d (5.4)	6.89 m (7.4)[g]			21	**38**	**To4$_{ipso}$**	139.92 d (2.3)
14	**To4d**	131.44 bs	6.93 m (7.5)[g]	Me4o		2/11			
15	**To3d**	131.08 d (6.6)	6.95 m[g]	Me3o		4/10/34	**39**	**To3$_{ipso}$**	140.14 d (13.5)
16	**To2p**	129.41 s	6.97 m (7.4)[g]			29/37			
17	**To3p**	127.49 s	6.98 m (7.8)[g]			9/39	**40**	**To1$_{ipso}$**	141.10 d (14.3)
18	**To1o**	129.76 d (~2)	7.01 m[f][g]		To4o	24/40			
19	**Ph5m**	128.36 d (8.9)	7.10 m[g]			19/26/35			
20	**To4p**	129.59 s	7.14 m (7.5)[g]		To1p	14/28/38			
21	**To1d**	131.47 d (3.7)	7.14 m (7.2)[g]	Me1o		5/13/33			
22	**Ph6m**	128.10 d (9.2)	7.22 m (~7)[g]			36			
23	**Ph6p**	128.79 s	7.22 m (~7)[g]			36			
24	**To1p**	128.65 s	7.23 m (7.4/7.2)[g]		To4p	13/18/33/40			
25	**Ph5p**	128.96 s	7.24 m[g]			26/35			
26	**Ph5o**	130.80 d (12.9)	7.40 pt (7.8)[f]	Me3A/B	Ph6o	25/26/35			
27	**Ph6o**	130.22 d (12.3)	7.49 pt (6.8)[f]	Me3A/B/Me1A	Ph5o	23/27/36			
28	**To4o**	138.62 d (34.1)	7.57 dd (7.6)[f]		To1o	2/14/20/38			
29	**To2o**	138.98 d (35.3)	7.72 dd (7.8)[f]	Me1o	To3o	3/12/16/37			

[a] The numbering scheme refers to Figure 3 with the following addenda: MeX denotes the carbon atom of the methyl group on the ligand backbone; Npq refers to the quaternary carbon atom of the neopentane backbone; Meαo_{ipso} refers to the carbon atoms of the *o*-tolyl group α (α = 1−4) bearing the methyl substituent; Toα_{ipso} denotes the corresponding *ipso* carbon atom of the *o*-tolyl groups, while Phβ_{ipso} (β = 5−6) analogously denotes the *ipso* carbon atoms of the phenyl groups. − [b] $^nJ_{CP}$ in Hz is given in brackets. − [c] $^{2/3}J_{HH}$ in Hz is given in brackets. − [d] $^1J_{CH}$ = 127.1 Hz. − [e] $^1J_{CH}$ = 127.8 Hz. − [f] $^nJ_{HP}$ = 5.1 Hz (Me3B); 8.7 Hz (Me2B); 8.4 Hz (Me1B); 5.9 Hz (Me1A); 10.4 Hz (Me3A); 6.7 Hz (Me2A); 8.3 Hz (To3o); 7.7 Hz (To1o); 8.8 Hz (Ph5o); 7.9 Hz (Ph6o); 17.3 Hz (To4o); 17.5 Hz (To2o). − [g] Signals of individual groups overlap; $^3J_{HH}$ coupling constants were determined by DQF-COSY experiments.

ing an analogous procedure to the complete set of data for **2** leads to an estimate of $\Delta H^{\neq}$ (R^2 = 0.990, $\Delta H^{\neq}$ = 48.7 ± 0.7 kJ·mol^{-1}; limits refer to σ; Table 1) in satisfying agreement with the value derived from the line-shape analysis data alone. The estimated activation entropy, however, is about 10 J·K^{-1}·mol^{-1} more negative ($\Delta S^{\neq}$ = −31 ± 3 J·K^{-1}·mol^{-1}; limits refer to σ; Table 1) than that obtained by using data solely from the line-shape analysis (see above, $\Delta S^{\neq}$ = −20 ± 2 J·K^{-1}·mol^{-1}; limits refer to σ; Table 1). This discrepancy between the $\Delta S^{\neq}$ values estimated on the basis of the two different data sets (line-shape analysis data alone vs. augmented data set) is close to the three σ limit, which is conventionally used to discriminate between equality or inequality of the statistical distribution that two items are subject to. It is thus found that, within the appropriate confidence interval, the two different approaches used generate estimates which, as expected, can be taken as equal. As judged from the scatter of data, the activation parameters derived from line-shape analysis alone are the most reliable, and hence these data have been quoted for **1** and **2** wherever appropriate in the text; Table 1 contains both types of estimates. To sum up, it appears that the line-shape analysis produces the most reliable data. It is felt that the data derived from EXSY measurements are less reliable, where different types of biases may result from overlap of peaks along the diagonal, NOE contributions, and loss of polarization during different delays. Likewise, coalescence data do not appear to be as reliable as the data obtained from line-shape analysis in the specific cases studied. Estimating the coalescence temperature is a procedure which is subject to personal judgement. Coupling between the coalescing nuclei makes this process even more subject to human error.

Finally, it is felt that the NMR work reported herein has some importance beyond the specific chemistry studied in this paper since the utility and reliability of three NMR techniques for the assessment of rate constants have been compared in the analysis of one and the same problem.

Force Field Calculations: Programs and parameters have been described previously,[10] as have the protocols of the individual computational procedures.[12] Details relating to the scanning of the hypersurface are given explicitly in the text. All computations were performed on a Silicon Graphics Indigo^2 MIPS R4400 workstation, 200 MHz, 128 MB RAM, operating under IRIX 5.3. Graphical representations of hypersurfaces were obtained using the *plot2D* option of MacroModel.[27]

Synthetic Procedures

1-[Bis(*o*-tolyl)phosphanyl]-3-(diphenylphosphanyl)-2-(diphenylphosphanylmethyl)-2-methylpropane (1a): To a solution of 1.3 g (2.8 mmol) of 1-chloro-2-bis(diphenylphosphanylmethyl)propane[28] in DMSO (50 mL), 730 mg (3.4 mmol) of bis(*o*-tolyl)phosphane and 380 mg (3.4 mmol) of KO*t*Bu were added and the mixture was stirred for 3 h at 130°C. The reaction mixture was worked-up hydrolytically by adding water (50 mL) and then neutralizing

Table 14. ^{1}H- and ^{13}C{^{1}H}-NMR data of **1**; the meaning of symbols is as in Figure 2

	NMR spectra			Correlations			Data for quaternary carbons		
No	Nucleus[a]	δ(^{13}C)[b]	δ(^{1}H)[c]	NOESY	EXSY	HMBC	No	Nucleus[a]	δ(^{13}C)[b]
1	MeX	39.43 q (9.2)	1.46 bs			4/5/6/27	27	Npq	36.60 q (6.5)
2	Me2o	21.15[d] d (2.3)	1.51 s	To2d	Me1o	2/8/11/29/34			
3	Me1o	21.15[d] d (8.6)	1.77 s	To1d	Me2o	3/7/9/12/28/34	28	Me1o$_{ipso}$	133.52 dd (4.9/31.8)
4	Me3A	30.59 pt (12.5)	1.82 dd (15.6)[e]		Me2B	5/6/27/31/33			
5	Me2A	33.87 pt (12.3)	2.02 dd (14.9)[e]	Ph3o	Me3B	4/6/27/30/32	29	Me2o$_{ipso}$	134.13 dd (3.3/26.0)
6'	Me1B	34.38 pt (11.1)	2.17 pt (15.2)[e]		Me1A	1/4/27/29			
6	Me1A	34.38 pt (11.1)	2.51 dd (15.2)[e]	To1o	Me1B	4/5/27/28/29	30	Ph4$_{ipso}$	137.50 dd (4.0/26.7)
5'	Me2B	33.87 pt (12.3)	2.60 ddd (14.9)[e]		Me3A	1/6/27/30/32			
4'	Me3B	30.59 pt (12.5)	2.76 ddd (15.6)[e]	Ph6o	Me2A	1/5/27/31/33	31	Ph6$_{ipso}$	137.91 dd (6.0/25.8)
7	To1o	126.31 dd (1.0/3.6)	6.03 pt (7.3)[e]	Me1A/B/Me2o	To2o	3/13/34			
8	To2m	124.65 d (16.3)	6.26 pt (7.4)		To1m	11/15/26/29/34	32	Ph3$_{ipso}$	138.30 dd (6.5/33.4)
9	To1m	124.4 d (6.3)1	6.47 pt (7.4)		To2m	7/12/13/28/34			
10	Ph4m	127.58 d (9.2)	6.86 pt (7.5)		Ph5m	10/14/23/30	33	Ph5$_{ipso}$	138.47 dd (6.5/33.4)
11	To2d	131.63 d (4.6)	6.92 d (7.5)	Me2o		2/8/15/29/34			
12	To1d	130.67 d (8.3)	6.96 dd (7.5)[e]	Me1o		3/9/28/34	34	To2$_{ipso}$	139.52 d (1.7)
13	To1p	127.44 s	7.02 pt (7.3)			7/9/28/34			
14	Ph4p	128.65 s	7.07 d (6.8)		Ph5p	10/23	35	To1$_{ipso}$	140.02 d (13.8)
15	To2p	129.56 s	7.08 d (7.3)			26/29/34			
16	Ph5m	127.78 d (9.5)	~7.17 m (7.6)[f]		Ph4m	16/20/33			
17	Ph6m	128.33 d (8.9)	~7.20 m (7.6)[f]		Ph3m	17/25/31			
18	Ph5p	128.41 bs	~7.23 m[f]		Ph4p	20			
19	Ph6p	128.99 s	~7.31 m[f]			25			
20	Ph5o	130.04 d (12.6)	7.32 m (7.8)[e][f]			18/20			
21	Ph3p	128.76 s	~7.39 m[f]			22/24/32			
22	Ph3m	128.04 d (8.9)	~7.40 m[f]		Ph6m	22/24/32			
23	Ph4o	131.76 d (13.8)	7.40 m (7.7)[f]			14/23			
24	Ph3o	130.51 d (11.5)	7.58 m (7.3)[e][f]	Me2A		21/24			
25	Ph6o	130.58 d (13.5)	7.58 m (7.3)[e][f]	Me3B		19/25			
26	To2o	138.23 d (35.0)	7.64 dd (7.5)[e]	Me2A	To1o	2/15/34			

[a] The numbering scheme refers to Figure 2 with the following addenda: MeX denotes the carbon atom of the methyl group at the backbone of the ligand; Npq refers to the quaternary carbon atom of the neopentane backbone; Meαo$_{ipso}$ refers to the carbon atoms of the *o*-tolyl group α (α = 1−2) bearing the methyl substituent; Toα$_{ipso}$ denotes the corresponding *ipso* carbon atom of the *o*-tolyl groups, while Phβ$_{ipso}$ (β = 3−6) analogously denotes the *ipso* carbons of the phenyl groups. − [b] $^nJ_{CP}$ in Hz is given in brackets. − [c] $^{2/3}J_{HH}$ in Hz is given in brackets. − [d] $^1J_{CH}$ = 126.9 Hz. − [e] $^nJ_{HP}$ = 2.6 Hz (Me3A); 2.2 Hz (Me2A); 12.7 (Me1B); 4.8 Hz (Me1A); 10.7 Hz (Me2B); 11.2 Hz (Me3B); 8.2 Hz (To1o); 4.2 Hz (To1d); 10.4 Hz (Ph5o); 9.7 Hz (Ph3o/Ph6o); 17.7 Hz (To2o). − [f] Signals of individual groups overlap; $^3J_{HH}$ coupling constants were determined by DQF-COSY experiments.

with 37% aq. HCl. The product was extracted with diethyl ether (4 × 50 mL) and the combined organic phases were dried and concentrated in vacuo. The resulting pasty residue was purified by column chromatography on silica gel (20 cm, Ø = 5 cm) using petroleum ether (40/60)/diethyl ether (9:1) as eluent (TLC control, R_f = 0.50) to yield 1.7 g (2.7 mmol, 95%) of ligand **1a** as a colorless oil.

1-[Bis(*o*-tolyl)phosphanyl]-3-(diphenylphosphanyl)-2-(diphenylphosphanylmethyl)-2-methylpropanetricarbonylmolybdenum (1): To a solution of 1.7 g (2.7 mmol) of **1a** in CH_2Cl_2 (50 mL), 815 mg (2.7 mmol) of solid $(MeCN)_3Mo(CO)_3$[29] was added and the mixture was stirred for 2 h at room temperature. During the course of the reaction, the $(MeCN)_3Mo(CO)_3$ slowly dissolved and the color of the solution turned from light-yellow to yellow-brown. The solvent was then removed to leave a brown solid. The crude product was purified by column chromatography on silica gel (10 cm, Ø = 4 cm) using a mixture of petroleum ether (40/60)/CH_2Cl_2 (1:3) as eluent (TLC control: R_f = 0.75) to afford 1.5 g (1.8 mmol, 67%) of **1** as a light-yellow microcrystalline solid. The product was recrystallized from CH_2Cl_2. − IR (CH_2Cl_2): $\tilde{\nu}$ = 1936 (s, CO), 1844 (br. s, CO). − MS(EI); *m/z* (%): 834 (10) [M^+], 806 (12) [M^+ − CO], 778 (40) [M^+ − 2 CO], 750 (30) [M^+ − 3 CO].

1,1,1-Tris[bis(*o*-tolyl)phosphanylmethyl]ethane (3a): 3.87 g (18 mmol) of bis(*o*-tolyl)phosphane[30] was dissolved in DMSO (25 mL) and deprotonated at 0°C by adding 2.02 g (18 mmol) of KO*t*Bu. After warming to room temperature, the deep-red solution was stirred for 1 h. A solution of 0.92 g (5.25 mmol) of 1-chloro-2,2-dichloromethylpropane in DMSO (25 mL) was then slowly added and the resulting mixture was refluxed for 5 h. The mixture was then cooled to room temperature and the DMSO was evaporated in vacuo. The residue was hydrolyzed by adding degassed water (50 mL). After stirring for 16 h, **3a** was extracted with diethyl ether (4 × 50 mL). The combined organic phases were dried over $MgSO_4$ and filtered. Evaporation of the solvent afforded 2.3 g (3.2 mmol, 62%) of **3a** as a white powder; m.p. 176°C. − ^{1}H NMR ($CDCl_3$): δ = 1.1 (s, 3 H, CqCH_3), 2.4 (m, 24 H, ArCH_3, CH_2P), 7.10−7.33 (m, 24 H, arom. H). − ^{13}C NMR ($CDCl_3$): δ = 20.8 (s, Ar*C*H$_3$), 21.3 (s, Ar*C*H$_3$), 42.5 (m, Cq), 125.0−142.2 (m, arom. C). − ^{31}P NMR ($CDCl_3$): δ = −50.9 (s). − MS (FAB); *m/z* (%): 708 (32) [M^+], 617 (100) [M^+ − (*o*-tolyl)], 495 (16) [M^+ − P(*o*-tolyl)$_2$].

1,1,1-Tris[bis(*o*-tolyl)phosphanylmethyl]ethanetricarbonylmolybdenum (3): 708 mg (1 mmol) of the ligand **3a** was dissolved in CH_2Cl_2 (30 mL) and this solution was added to 333 mg (1.1 mmol) of solid $(CH_3CN)_3Mo(CO)_3$[29] at 20°C. The resulting mixture, which immediately turned dark, was stirred for 48 h. Petroleum ether (40/60) (6 mL) was then added and the mixture was filtered through silica gel (2 cm) and Kieselgur (1 cm), resulting in a yellow eluent. Evaporation of the solvent and drying of the residue in vacuo for 48 h afforded 835 mg (0.94 mmol, 94%) of **3** as a pale-yellow powder. A reagent tube filled with a concentrated solution of **3** in CH_2Cl_2 was placed in a Schlenk tube containing a bottom layer of diethyl ether. Vapour diffusion of the diethyl ether at room temperature yielded pale-yellow crystals suitable for X-ray structural analysis within one day.[10] − IR ($CHCl_3$): $\tilde{\nu}$ = 1932 (s, CO), 1835 (br. s, CO). − ^{1}H NMR ($CDCl_3$): δ = 1.65 (m, 3 H, CqCH_3), 1.75−2.0 (m, 18 H, ArCH_3), 2.0−3.0 (br. m, 6 H, CH_2P), 6.5 (m, 6 H, arom. H), 6.8−7.5 (m, 18 H, arom. H). − ^{13}C NMR ($CDCl_3$):

δ = 22.31 (m, Ar*C*H$_3$), 23.22 (m, Ar*C*H$_3$), 38.9 (m, *C*H$_2$P), 42.0 (m, Cq), 125.0−141.3 (m, arom. C), 220 (s, CO). − ^{31}P NMR (CDCl$_3$): δ = 20.0 (s).

Acknowledgments

The financial support by the Deutsche Forschungsgemeinschaft (SFB 247, Normalverfahren HU 151/24-1, /29-1) and the Fonds der Chemischen Industrie is gratefully acknowledged. We are indebted to Mr. T. Jannack for performing mass spectrometric measurements and to the staff of the Microanalytisches Labor of the Organisch-Chemisches Institut, Heidelberg, for providing microanalyses. We wish to acknowledge the early inspiration by the Deutsches Museum, München.

[1] G. Frenking, I. Antes, M. Boehme, S. Dapprich, A. W. Ehlers, V. Jonas, A. Neuhaus, M. Otto, R. Stegmann, A. Veldkamp, S. F. Vyboishchikov, in: *Reviews in Computational Chemistry*, vol. 8 (Eds.: K. B. Lipkowitz, D. B. Boyd), VCH Publishers, Inc., New York, **1996**, chapter 2.
[2] L. J. Bartolotti, K. Flurchick, in: *Reviews in Computational Chemistry*, vol. 7 (Eds.: K. B. Lipkowitz, D. B. Boyd), VCH Publishers, Inc., New York, **1996**, chapter 4.
[3] N. L. Allinger, *J. Am. Chem. Soc.* **1977**, *99*, 8127−8134.
[4] U. Burkert, N. L. Allinger, *Molecular Mechanics*, ACS monograph, Washington DC, **1992**.
[5] P. Comba, T. W. Hambley, *Molecular Modelling of Inorganic Compounds*, VCH, Weinheim, **1995**.
[6] B. J. Hay, *Coord. Chem. Rev.* **1993**, *126*, 177−236.
[7] C. R. Landis, D. M. Root, T. Cleveland, in: *Reviews in Computational Chemistry*, vol. 6 (Eds.: K. B. Lipkowitz, D. B. Boyd), VCH Publishers, Inc., New York, **1995**, chapter 2.
[8] S. Beyreuther, J. Hunger, G. Huttner, S. Mann, L. Zsolnai, *Chem. Ber.* **1996**, *129*, 745−757.
[9] G. Huttner, S. Beyreuther, J. Hunger, in: *Software-Entwicklung in der Chemie 10* (Ed.: J. Gasteiger), GDCH, Frankfurt, **1996**, p. 201−207.
[10] J. Hunger, S. Beyreuther, G. Huttner, K. Allinger, U. Radelof, L. Zsolnai, *Eur. J. Inorg. Chem.* **1998**, 693−702.
[11] J. Hunger, G. Huttner, *J. Comput. Chem.* **1999**, *20*, 455−471.
[12] S. Beyreuther, J. Hunger, S. Cunskis, T. Diercks, A. Frick, E. Planker, G. Huttner, *Eur. J. Inorg. Chem.* **1998,** 1641−1653.
[13] [13a] U. Piantini, O. W. Sørensen, R. R. Ernst, *J. Am Chem. Soc.* **1982**, *104*, 6800−6801. − [13b] M. Rance, O. W. Sørensen, G. Bodenhausen, G. Wagner, R. R. Ernst, K. Wüthrich, *Biochem. Biophys. Res. Commun.* **1983**, *117*, 479−485.
[14] [14a] L. Braunschweiler, R. R. Ernst, *J. Magn. Res.* **1983**, *53*, 521−528. − [14b] A. Bax, D. G. Davis, *J. Magn. Res.* **1985**, *65*, 355−360.
[15] J. Jeener, B. H. Meier, P. Bachmann, R. R. Ernst, *J. Chem. Phys.* **1979**, *71*, 4546−4563.
[16] [16a] G. Bodenhausen, D. J. Ruben, *Chem. Phys. Lett.* **1980**, *69*, 185−188. − [16b] L. E. Kay, P. Keifer, T. Saarinen, *J. Am. Chem. Soc.* **1992**, *114*, 10663−10665. − [16c] A. G. Palmer III, J. Cavanagh, P. E. Wright, M. Rance, *J. Magn. Res.* **1991**, *93*, 151−170. − [16d] J. Schleucher, M. Schwendinger, M. Sattler, P. Schmidt, O. Schedletzky, S. J. Glaser, O. W. Sørensen, C. Griesinger, *J. Biomol. NMR* **1994**, *4*, 301−306.
[17] A. Bax, M. F. Summers. *J. Am Chem. Soc.* **1986**, *108*, 2093−2094.
[18] [18a] G. Binsch, *J. Am. Chem. Soc.* **1969**, *91*, 1304−1309. − [18b] WIN-DYNAMICS 1.0 Release 951220, NMR Dynamic Spectra Simulation and Iteration, Bruker-Franzen Analytik GmbH and K. Il′yasov, O. Nedopekin, Bremen, Germany.
[19] G. Binsch, H. Kessler, *Angew. Chem.* **1980**, *92*, 445−463; *Angew. Chem. Int. Ed. Engl.* **1980**, *19*, 411−429.
[20] J. Sandström, *Dynamic NMR Spectroscopy*, Academic Press, London, **1982**, chapter 7.
[21] C. L. Perrin, T. J. Dwyer, *Chem. Rev.* **1990**, *90*, 935−967.
[22] J. W. Goethe, *Goethe's Werke, Vollständige Ausgabe letzter Hand*, Cottasche Buchhandlung, Stuttgart und Tübingen, **1829**, vol. 22, p. 254, Betrachtungen im Sinne der Wanderer: "Germans, and not only them, are gifted to make science incomprehensible."
[23] For the meaning of the terms "one-ring flip" and "two-ring flip", see ref.[8]
[24] The approach used (*mm2f*, *mm2t*) makes use of the well-scaled force constants of the MM2*[3] force field for the organic part of the molecules. On the other hand, the force constants describing the "inorganic interactions" have been deduced by a minimization procedure based wholly on structural information.[10][11] There is, of course, no direct reference to energetic terms in such a structural database and if the force constants derived from this database are still appropriate on the energy scale, this must result from the indirect constraints imposed on them in the course of their refinement by the dominant force field contribution of the organic part. It was expected that the force constants used for the organic part might automatically force the refinement of the inorganic force field constants to the appropriate scale, as is indeed found.[12]
[25] E. W. Hansen, *Anal. Chem.* **1985**, *57*, 2993−2994.
[26] A. L. Van Geet, *Anal. Chem.* **1970**, *42*, 679−680.
[27] MacroModel 5.0 (MM2*) (see: F. Mohamadi, N. G. J. Richards, W. C. Guida, R. Liskamp, M. Lipton, C. Caufield, G. Chang, T. Hendrickson, W. C. Still, *J. Comput. Chem.* **1990**, *11*, 440−467).
[28] G. Reinhard, R. Soltek, G. Huttner, A. Barth, O. Walter, L. Zsolnai, *Chem. Ber.* **1996**, *129*, 97−108.
[29] [29a] W. S. Tsang, D. W. Meek, A. Wojcicky, *Inorg. Chem.* **1968**, *7*, 1263−1268. − [29b] D. B. Tate, W. R. Knipple, J. M. Augl, *Inorg. Chem.* **1962**, *1*, 433−434.
[30] [30a] F. G. Mann, E. J. Chaplin, *J. Chem. Soc.* **1937**, 527−535. − [30b] G. P. Schiemenz, *Angew. Chem.* **1968**, *80*, 559−560; *Angew. Chem. Int. Ed. Engl.* **1968**, *7*, 544−545. − [30c] Ch. A. Tolman, *J. Am. Chem. Soc.* **1970**, *92*, 2956−2965.

Received July 26, 1999
[I99272]